The response of high density turbidity currents and their deposits to an abrupt channel termination at a slope break: Implications for channel–lobe transition zones

Article *in* Sedimentology · January 2023

DOI: 10.1111/sed.13073

7 authors, including:

Jonathan Wilkin
University of Dundee
7 PUBLICATIONS 0 CITATIONS
SEE PROFILE

Alan Cuthbertson
University of Dundee
79 PUBLICATIONS 468 CITATIONS
SEE PROFILE

Sue Dawson
University of Dundee
67 PUBLICATIONS 2,203 CITATIONS
SEE PROFILE

Dorik A. V. Stow
Heriot-Watt University
309 PUBLICATIONS 509 CITATIONS
SEE PROFILE

SEDIMENTOLOGY the journal of the International Association of Sedimentologists

Sedimentology (2023) doi: 10.1111/sed.13073

The response of high density turbidity currents and their deposits to an abrupt channel termination at a slope break: Implications for channel–lobe transition zones

JONATHAN WILKIN*, ALAN CUTHBERTSON*, SUE DAWSON†,‡, DORRIK STOW§, KARL STEPHEN§, UISDEAN NICHOLSON§ and NADIA PENNA¶

**School of Science and Engineering (Civil Engineering), University of Dundee, Nethergate, Dundee, DD1 4HN, UK (E-mail: jzwilkin@dundee.ac.uk)*

†Division of Energy, Environment and Society, School of Humanities, Social Sciences and Law, University of Dundee, Nethergate, Dundee, DD1 4HN, Scotland

‡UNESCO Centre for Water Law, Policy and Science, University of Dundee, Nethergate, Dundee, DD1 4HN, Scotland

§Institute of GeoEnergy Engineering, Heriot Watt University, Campus The Avenue, Edinburgh, EH11 4AS, UK

¶Dipartimento di Ingegneria Civile, Università della Calabria, Via Pietro Bucci, 87036 Arcavacata CS, Rende, Italy

Associate Editor – Victoria Valdez

ABSTRACT

The transition between the slope and basin floor is typically marked by a slope break, in some cases causing channels to terminate and turbidity currents to undergo a loss of confinement. It is thus essential to understand how these slope breaks and losses of confinement influence the hydrodynamic evolution of turbidity currents and impact their depositional variability within natural scale channel mouth settings. Flume experiments, utilizing Shields scaling, are conducted to study how channel slope angle (3°, 6° and 9°) and initial suspended sediment concentrations (12 to 18% by volume) impact the hydrodynamics and deposit geometries of high density turbidity currents, subject to a simultaneous break of slope and loss of confinement. Measured velocity and concentration profiles indicate that turbidity currents are supercritical, with mean velocities between 0.80 m s^{-1} and 1.04 m s^{-1} and depth-averaged basal concentrations between 9.2% and 23.9%, yielding bed shear velocities between 0.050 m s^{-1} and 0.064 m s^{-1}. Upon encountering the slope break and loss of confinement, turbidity currents exhibit increases to their densimetric Froude numbers and shear velocities. This is due primarily to two factors: firstly, turbidity currents continue to accelerate during an initial period of velocity lag as their residual momentum gradually dissipates; and, secondly, expansion via flow relaxation collapses their structure towards the bed. The corresponding depositional geometries of these processes reveal that turbidity currents produce elongate channel–lobe transition zones that disconnect channel and basin deposits. The length to width ratios of channel–lobe transition zones decrease as the initial sediment concentrations of turbidity currents increase, while a reduction in the channel slope break angle reduces their length to width ratios. Corresponding, lobe elements are observed to increase in length, width and thickness with increasing initial sediment concentrations, while a reduction in channel slope break angle reduces their dimensions due to enhanced slope deposition.

Keywords Channel–lobe transition zone, flume experiments, high density turbidity currents, lobe element, loss of confinement, slope break.

INTRODUCTION

Turbidity currents (TCs) are particle-laden density flows that travel down slopes due to their excess density (i.e. due to suspended sediment particles combined with the interstitial fluid). These currents are capable of transporting large volumes of sediment (Stevenson *et al.*, 2018; Talling *et al.*, 2022), organic matter (Hage *et al.*, 2020) and anthropogenically-derived particles, such as microplastics (Kane & Clare, 2019; Pohl *et al.*, 2020a; Bell *et al.*, 2021), into deep oceanic basins. When TCs occur on slopes that are sufficiently steep they begin to bypass their sediment load, and, if erosive, will incise channels into these slopes (Fildani *et al.*, 2013; de Leeuw *et al.*, 2016). These channels then serve as future sediment transport conduits enabling less erosive turbidity currents to also bypass slope regions (Stevenson *et al.*, 2015) and deposit their suspended sediment in more distal, low-angle basin floor settings.

This switch to deposition takes place via a channel mouth that often coincides with areas in which TCs encounter topographic slope breaks (SB) (Hodgson *et al.*, 2022), such as the mouth of the Rhone Canyon, where there is a slope reduction of 0.3° (Wynn *et al.*, 2002). The recent study by Hodgson *et al.* (2022) identifies four key channel mouth settings: (i) channel mouth expansion zones dominated by supercritical turbidity currents; (ii) plunge pools that mark the base of steep slopes and are also created by supercritical turbidity currents; (iii) channel–lobe transition zones at shallower slope breaks characterized by hydraulic jump arrays within turbidity currents that have Froude numbers close to unity; and (iv) subcritical channel–lobe transition zones related to slope breaks and/or flow expansion.

Within channel mouth settings, TCs undergo a loss of confinement (LOC) and flow relaxation (Pohl *et al.*, 2019), spreading out laterally as they are no longer supported within the confined channel. This lateral spreading has the effect of lowering the height of maximum velocity within TCs towards the bed, promoting sediment bypass and enhancing basal shear stresses at the flow–bed interface. This results in the formation of scour regions that are prevalent features in both ancient (Macdonald *et al.*, 2011a; Ito *et al.*, 2014; Pemberton *et al.*, 2016; Brooks *et al.*, 2018b, 2022; Navarro & Arnott, 2020; Rohais *et al.*, 2021) and modern (Wynn *et al.*, 2002; Macdonald *et al.*, 2011b; Carvajal *et al.*, 2017; Maier *et al.*, 2020) channel–lobe transition zones (CLTZs). The dimensions of these scour regions range between metre and kilometre scales (Hofstra *et al.*, 2015) and are maintained by subsequent turbidity currents that can remain active for <0.2 Myr (Macdonald *et al.*, 2011a).

On slopes with complex localized topography, severe SBs can occur more often as a result of the surface expression of complex subsurface processes (Soutter *et al.*, 2021), leading to the formation of: (i) ponded accommodation (Spychala *et al.*, 2015); (ii) slopes with stepped profiles, such as mid-slope terraces (Brooks *et al.*, 2018a); (iii) seafloor topography resulting from geological folds (Howlett *et al.*, 2019) and exposed faults (Ge *et al.*, 2017); (iv) active salt diapirism (Howlett *et al.*, 2020; Cumberpatch *et al.*, 2021); and (v) at the base of steep continental margins (Lee *et al.*, 2002). Localized topographic variations are therefore important as they induce rapid shifts in the hydrodynamics of TCs that alter their depositional patterns on both local (Amy *et al.*, 2007; Patel *et al.*, 2021) and regional (Soutter *et al.*, 2019) scales. It is clear from previous studies that channel slope breaks have a different overall impact on the hydrodynamics of TCs than a loss of confinement. As such, many past experimental studies have focused on these two key geometric characteristics separately. For example, slope breaks have been shown to induce internal hydraulic jumps as the two-dimensional TCs transfer from a sloping to horizontal channel bed (Garcia & Parker, 1989; Mulder & Alexander, 2001). Similarly, while slope breaks occurring between two differential sloping channel beds typically result in the thickening of the TC wall region, the corresponding densimetric Froude numbers for the TCs may remain within the supercritical regime downstream of the SB (Pohl *et al.*, 2020a, 2022). By contrast, turbidity currents that undergo a LOC typically experience a two to three-dimensional transition in their hydrodynamic characteristics, primarily associated with a flow relaxation after the LOC that drives lateral expansion of the TCs into an unconfined basin (Pohl *et al.*, 2019).

This current study utilizes the Shields scaling technique (e.g. de Leeuw *et al.*, 2016, 2018; Pohl *et al.*, 2019, 2020a,b; Ferguson *et al.*, 2020; Miramontes *et al.*, 2020; Spychala *et al.*, 2020) to study the combined effect of SBs and LOCs on TCs that are capable of bypassing sediment. Previous studies that have combined SBs and LOCs have revealed that not all TCs decelerate immediately downstream of a simultaneous SB-LOC (Kostic & Parker, 2006). In some cases, the TCs remain within a supercritical flow regime (at least temporarily), meaning that they do not produce a stationary hydraulic jump immediately downstream of the SB-LOC (Alexander *et al.*, 2008; Pohl *et al.*, 2019, 2020b). The current study investigates the roles that slope break angle at the simultaneous SB-LOC and the initial suspended sediment concentration have on the hydrodynamics of the TCs generated and their resulting deposition patterns. This will address some of the outstanding questions on the specific hydrodynamic conditions of TCs that form erosional and depositional features within abrupt simultaneous SB-LOC settings. Previous analogies have been drawn to the impact pools produced by snow avalanches (Lee *et al.*, 2002) that are attributed to stationary internal hydraulic jumps (Dorrell *et al.*, 2016; Guiastrennec-Faugas *et al.*, 2021) or to flow relaxation due to loss of confinement.

Whether attached or detached from the slope, the deposits of channel mouth settings represent condensed stratigraphic intervals formed by the complex interplay of erosion, deposition and bypass (Gardner et al., 2003, 2008). When this stratigraphic complexity is coupled with the relatively poor preservation potential (Brooks *et al.*, 2018b) of channel mouth settings, it can be difficult to establish the hydrodynamic processes that produced bypass and erosion when the zones were active. That said, the sediments found in both ancient and modern CLTZs do provide an opportunity to understand the depositional processes in zones of flow expansion. For example, Mutti (1974, 1977, 1985) and Mutti & Normark (1987) identified channel mouth bypass zones and bars within deep-water systems, deducing that the dynamics, magnitude and frequency of TCs are likely to alter the spatial extent and preserved sedimentology. More recently, the criticality of TCs (Postma *et al.*, 2016), relative change in slope gradient (Van der Merwe *et al.*, 2014; Pohl *et al.*, 2020b), basin character (Garnder *et al.*, 2008) and sediment granulometry and mineralogy (Navarro & Arnott, 2020) have all been shown to impact on the geometries of channel mouth deposits. In this regard, experimental studies are therefore highly beneficial to the fundamental understanding of these relationships because they permit both geometrical simplification of complex channel–basin systems and control over key parameters. This provides a means of assessing the relationships that exist between the hydrodynamics and deposits of TCs within channel mouth settings.

The current study presents results from carefully controlled laboratory experiments that study the influence of suspended sediment concentration and slope break angle on the hydrodynamics of TCs within a CLTZ that forms as the TCs encounter a simultaneous and abrupt SB-LOC. The study also assesses the geometrical properties of deposits produced prior to and after the TCs encounter the SB-LOC (i.e. within the sloping confined channel and on the horizontal unconfined basin floor, respectively).

EXPERIMENTAL METHODS

Flume channel–basin setup

The experiments are conducted in a purpose-built, Perspex-walled flume facility (Fig. 1) consisting of a straight 3.20 m-long, 0.1 m-wide and 0.3 m-high confined and sloping channel section that exits into a larger 2 m-long, 2 m-wide and 1 m-deep unconfined basin. The basin incorporates a raised, horizontal bed with overall dimensions 1.70 m-long × 1.50 m-wide × 0.11 m-high (Fig. 1), providing a trough around its perimeter to minimize flow reflections. The confined sloping channel bathymetry is adjustable between an along-channel bed slope $S_0 = 0$ and 0.176 (i.e. slope angle = 0–10°) and transitions abruptly at the SB-LOC onto the horizontal bed within the basin. In the initial experimental configuration, the channel–basin flume facility is filled with freshwater ($\rho_0 = 998$ kg m^{-3}) to a total water depth of 0.90 m corresponding to the fixed height of the syphon overflow in the basin that maintains the free surface elevation (Fig. 1). For the experiments reported in this study, each individual experimental run is conducted with initially sediment-free channel and basin bed conditions.

The TCs are generated at the upstream end of the sloping channel section by a pumped water–sediment feed through an inlet manifold of dimensions 0.044 m-high and 0.089 m-wide (Fig. 1B). Three series of experiments (Series S1, S2 and S3) consider different combinations of confined channel slope angle (i.e. 3°, 6° and 9°) and the volumetric suspended sediment concentration c_0 [i.e. 0.12, 0.14, 0.16 and 0.18 (12–18%)] at the source (see Table 1 for details). These conditions are chosen to ensure that velocities within the TCs are sufficiently high for erosion and sedimentological bypass to occur downstream of the SB-LOC location within the basin (Fig. 1C). The high initial

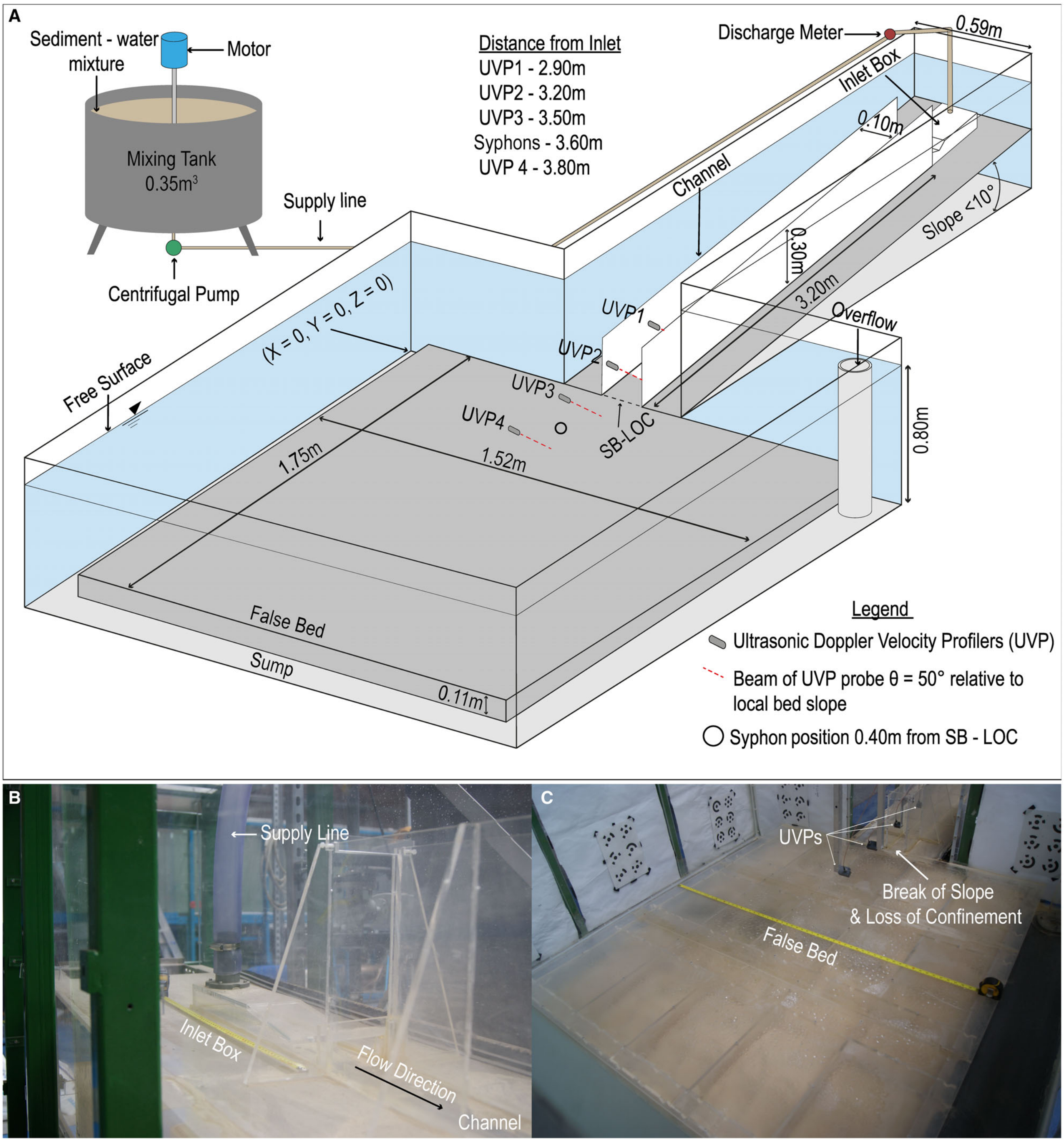

Fig. 1. (A) Schematic representation of the channel–basin facility used in the study, (B) inlet manifold configuration for high-density turbidity current (HDTC) generation, (C) unconfined, horizontal basin downstream of the slope break angle at a simultaneous loss of confinement (SB-LOC).

concentrations also mean that all experimental runs develop high-density turbidity currents (HDTCs) (Kuenen & Migliorini, 1950; Cartigny *et al.*, 2013). This is in accord with measurements of natural HDTCs (Paull *et al.*, 2018) that found basal volumetric concentrations to be >10%, meaning that sediment exchange between the HDTC and the bed within the scaled laboratory setting is likely to be governed by the same physical processes (i.e. hindered

Table 1. Details of the experimental studies highlighting the specific parameter variations associated with the initial source conditions (Q, c_0, u_0) and confined channel slope (i.e. slope break angle) considered within this study.

Expt. series	Run no.	Inlet volume flux Q ($m^3\ h^{-1}$: $l\ s^{-1}$)	Inlet velocity u_0 ($m\ s^{-1}$)	Average channel slope (°)	Volumetric sediment conc. c_0	Inlet Froude number Fr_D	Shear velocity U_* ($m\ s^{-1}$) (UVP2)	Rouse number ζ (D_{50}) (UVP2)
S1	R1.1	13.02: 3.62	0.92	9	0.12	3.16	0.0549	0.67
	R1.2	12.71: 3.53	0.90	9	0.14	2.86	0.0588	0.62
	R1.3	12.81: 3.56	0.91	9	0.16	2.69	0.0619	0.59
	R1.4	12.80: 3.56	0.91	9	0.18	2.54	0.0644	0.57
	R1.5	12.73: 3.54	0.90	9	0.12	3.09	–	–
	R1.6	12.75: 3.54	0.90	9	0.14	2.86	–	–
	R1.7	12.60: 3.50	0.89	9	0.16	2.65	–	–
	R1.8	12.78: 3.55	0.91	9	0.18	2.53	–	–
S2	R2.1	12.70: 3.53	0.90	6	0.12	3.08	0.0538	0.68
	R2.2	12.71: 3.53	0.90	6	0.14	2.86	0.0568	0.64
	R2.3	12.64: 3.51	0.90	6	0.16	2.66	0.0576	0.63
	R2.4	12.74: 3.54	0.90	6	0.18	2.52	0.0610	0.60
	R2.5	14.14: 3.93	1.00	6	0.12	3.43	–	–
	R2.6	13.78: 3.83	0.98	6	0.14	3.10	–	–
	R2.7	13.70: 3.81	0.97	6	0.16	2.88	–	–
	R2.8	13.70: 3.81	0.97	6	0.18	2.71	–	–
S3	R3.1	13.87: 3.85	0.98	3	0.12	3.37	0.0555	0.66
	R3.2	13.60: 3.78	0.96	3	0.18	2.69	0.0629	0.58
	R3.3	13.93: 3.87	0.99	3	0.12	3.38	–	–
	R3.4	13.94: 3.87	0.99	3	0.18	2.76	–	–

settling and grain-to-grain interactions) (Heerema *et al.*, 2020).

Flow scaling and characterization

The current experimental study is designed to investigate the transition between net depletive, sediment bypassing and erosive HDTCs at an abrupt SB-LOC. Shields scaling (Shields, 1936) is used to ensure that both the Shields parameter τ^* and the particle Reynolds number Re_p of the laboratory turbidity currents reside within appropriate flow regimes as those reported in natural HDTC systems. These parameters represent the ratio of bed shear stress to gravitational forces acting on the sediment and the hydrodynamic condition at the bed boundary of the HDTC, respectively. When these scaling conditions are satisfied, the laboratory HDTCs are able to erode and maintain suspended sediment transport in the downslope direction, as found in natural bypassing slope systems (Fig. 2), for example within the Monterey Canyon, USA (Xu *et al.*, 2014). The Shields parameter τ^* and particle Reynolds number Re_p are defined for the current study as:

$$\tau^* = \frac{\rho_t U_*^2}{(\rho_s - \rho_0) g\, D_{50}} \tag{1}$$

$$Re_p = \frac{U_* D_{50}}{v} \tag{2}$$

where $\rho_t = (\rho_s - \rho_w)\overline{c}_b + \rho_w$ is the density of the HDTC, v is the kinematic viscosity of water, g is the gravitational acceleration, D_{50} is the median grain size of the sediment within the flow and U_* is the shear velocity. Concentration $\overline{c}_b$ represents the time-averaged concentration in the near-bed region only (i.e. $\overline{c}_b$ between $z = 0$ and $z = H_{\max}$, where $H_{\max}$ is the layer thickness between the time average position of $U_{\max}$ relative to the bed). In order to calculate shear velocity U_*, this study assumes that a logarithmic velocity profile exists between the bed surface $z = 0$ and $z = H_{\max}$ within each HDTC (e.g. van Rijn, 1993), such that:

$$U_* = U_{\max}\, \kappa \left[\ln\left(\frac{H_{\max}}{0.1\, D_{90}}\right)\right]^{-1} \tag{3}$$

where κ is the von Kármán constant (= 0.41). It is noted that the value of v for the experimental

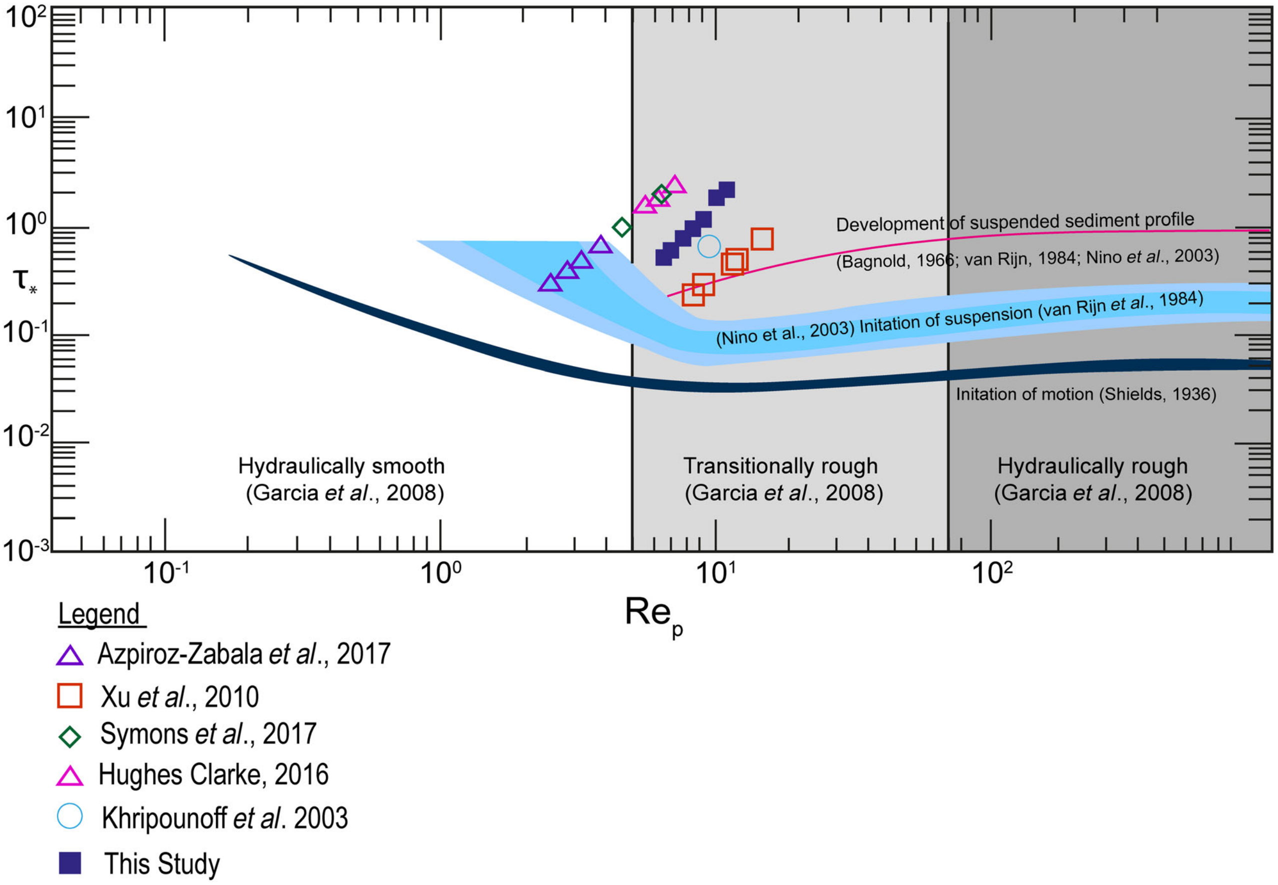

Fig. 2. Shields parameter τ_* (Eq. 1) plotted versus particle Reynolds numbers Re_p (Eq. 2) for the experimental data within this study for comparison with equivalent τ_* and Re_p values from field observations of naturally occurring turbidity currents (TCs). (Figure based on De Leeuw *et al.*, 2016; with data taken from Soutter *et al.*, 2021.)

flows is likely higher than that of the ambient water due to the addition of suspended sediment (Boyer *et al.*, 2011). However, this effect occurs equally within HDTCs at both the laboratory (Pohl *et al.*, 2020a,b) and field scales (Paull *et al.*, 2018) and is therefore not taken into account.

Within Shields scaling, the particle Reynolds number Re_p can be categorized as either hydraulically smooth ($\mathrm{Re}_p < 5$), transitionally rough ($5 < \mathrm{Re}_p < 70$) or rough ($\mathrm{Re}_p > 70$), with most natural scale HDTCs residing in the smooth to transitionally rough regimes (Fig. 2). The corresponding Shields parameter τ^* typically varies between 10^{-1} to 10^{0}, corresponding to flow conditions where a suspended sediment profile develops. Within the current experiments, the particle Reynolds numbers range between $\mathrm{Re}_p = 6.66$ to 12.38 (i.e. transitionally rough) and the corresponding Shields parameter ranges between $\tau^* = 0.66$ to 2.78. These experimental conditions thus reside within the same flow regimes as field measurements of natural TC systems (e.g. Xu *et al.*, 2004; Azpiroz-Zabala *et al.*, 2017; Zhang *et al.*, 2018).

It is also important to define the densimetric Froude number Fr_D of the HDTC at the source, and its spatial variation through the channel–basin system. This parameter defines the criticality of the HDTC flow regime, the evolution of which is crucial to understanding the hydrodynamic influence of the SB-LOC system. The densimetric Froude number Fr_D is defined as follows:

$$\mathrm{Fr}_D = \frac{\overline{U}}{\sqrt{g' h_{\max}}} \tag{4}$$

where $\overline{U}$ is the depth-averaged velocity in the HDTC, g' is the reduced gravitational acceleration defined as $g' = g[(\overline{\rho}_t - \rho_0)/\rho_0]$, with $\overline{\rho}_t = (\rho_s - \rho_w)\overline{c} + \rho_w$ being the depth-averaged

HDTC density at the concentration syphon location downstream of the SB-LOC, $\rho_0 = \rho_w$ the density of the ambient fluid, $\overline{c}$ the layer averaged volumetric concentration and ρ_s the sediment grain density. In Eq. 4, $h_{\max}$ is defined as the time-averaged thickness of the HDTC layer, determined by the elevation at which current velocity $U = 0.5U_{\max}$ (Launder & Rodi, 1983; Gray *et al.*, 2006). At the inlet manifold, the source velocity $u_0 = 0.89$ to 1.0 m s^{-1} and the current thickness $h = h_0 = 0.044$ m, with corresponding densimetric Froude numbers $\mathrm{Fr}_0 = u_0/(g_0' \ h_0)^{1/2} = 2.52$ to 3.43 (i.e. supercritical flow regime, see Table 1). Corresponding Reynolds numbers at the inlet (i.e. $\mathrm{Re} = 4u_0h_0/\nu$) range from 1.5×10^5 to 1.8×10^5 and therefore reside in the fully turbulent flow regime.

The Rouse number ζ, which defines the shape of the suspended sediment concentration profile within the evolving turbidity current, is also calculated for the D_{10}, D_{50} and D_{90} percentiles of the sediment grain-size distribution to assess the expected mode by which the initial sediment load within the TCs will be transported. The Rouse number ζ is given by:

$$\zeta = \frac{w_s}{\kappa U_*} \tag{5}$$

where w_s is the settling velocity of each of the individual grain-size percentiles, calculated using an empirical equation for natural sand particle settling (Cheng, 1997). In this way, the settling velocities for the D_{10} (95 μm), D_{50} (168 μm) and D_{90} (282 μm) grain sizes are calculated as $w_s = 0.005 \text{ m s}^{-1}$, 0.0147 m s^{-1} and 0.0311 m s^{-1}, respectively.

It is also informative to consider the energy balance within the HDTC between the confined, sloping channel and the unconfined, horizontal basin by calculating the potential energy E_p (Al Ja'Aidi *et al.*, 2004) and kinetic energy E_k per unit volume through the channel–basin system, as follows:

$$E_k = \frac{1}{2}\overline{\rho}_t\overline{\mathrm{U}}^2 \tag{6}$$

$$\mathrm{E}p = \frac{1}{2}\overline{\rho}_t g\left(\frac{\overline{\rho}_t - \rho}{\rho}\right)h_{\max} \tag{7}$$

Experimental procedure

Prior to each experimental run, the channel bed is set at the appropriate slope break angle and the channel–basin facility is filled in with freshwater. A sediment–water mixture volume (*ca* 350 l) with the appropriate volumetric suspended sediment concentration (Table 1) is stirred vigorously by a motorized impeller within an external circular mixing tank for 30 min to ensure homogeneity. The sediment used in the study is a moderately well-sorted fine quartz sand (Redhill 110, see Appendix S1) with a specific grain density $S_s = \rho_s/\rho_0 = 2.65$ (where $\rho_s = 2650 \text{ kg m}^{-3}$ is the sand grain density). The grain-size distribution for the sediment, measured by a laser particle size analyser (Malvern Mastersizer 2000; Malvern Panalytical, Malvern, UK), provides D_{10}, D_{50} and D_{90} percentiles of 90 μm, 163 μm and 284 μm, respectively.

The source volume flux inflow for the HDTCs is set constant at $Q = 3.66 \text{ l s}^{-1}$ ($\pm 0.15 \text{ l s}^{-1}$) for each individual experimental run (see Appendix S1). This inflow is generated from the water–sediment mixing tank via a centrifugal pump, with flow rate controlled by a ball valve, prior to delivery via a short supply pipe to the inlet manifold. In all experimental runs, inflow conditions are maintained over a 50 s run duration for each HDTC, with the discharge being monitored in the supply pipe by a magnetic flow meter (Siemens Mag6000, accuracy ±0.4% of flow rate, see Appendix S1 for discharge plots; Siemens, Munich, Germany).

Four ultrasonic velocimeter doppler profiler (UVP) probes (Met-Flow, UVP DUO, 2 MHz; Met-Flow SA, Lausanne, Switzerland) are positioned along the channel and basin centreline (Fig. 1) to record the evolving flow structure of the HDTCs throughout each experimental run (see Appendix S1 for UVP measurement parameters). To sample the main body region of the HDTCs, a data measurement window for the current is set such that the UVP probes are initiated 5 s after the passing of the HDTC head. The velocity measurements end 5 s before the termination of the sediment–water mixture at the inlet manifold and, thus, prior to the HDTC tail. The UVP probes are orientated at $\theta = 50°$ relative to the local bed slope and positioned at 2.90 m (UVP 1), 3.20 m (UVP 2), 3.50 m (UVP 3) and 3.80 m (UVP 4) downstream of the inlet manifold. As such, probes UVP 2 and UVP 3 are sited immediately upstream and downstream of the SB-LOC in the confined, sloping channel and unconfined, horizontal basin, respectively (see Fig. 1A). The UVP probes measure the velocity component U of the HDTCs along the probe measurement axis, with the along-channel, bed-parallel velocity u_x then calculated from $u_x = U/\cos\theta$. This assumes that 1D flow exists within the HDTCs along the channel–basin centreline, such that vertical and lateral flow velocity components are negligible in comparison to the streamwise component.

A number of repeat runs are conducted for specific experimental conditions (i.e. c_0 = 12–18% in Series S1, S2 and S3, see Table 1) to measure the vertical concentration structure of HDTCs within the bypass region, 0.4 m downstream of the SB-LOC (Fig. 1). Sediment concentration samples are syphoned at four elevations above the basin false bed (i.e. $z = 1$, 2, 4 and 8 cm in S1, and $z = 2$, 3, 5 and 9 cm in S2 and S3), with depth-averaged flow velocities from UVP3 used to adjust flow abstraction rates using peristaltic pumps to ensure that extraction velocities at the sampling pipe openings match the streamwise current flow velocities. Estimates of the vertical concentration profiles $c(z)$ for each HDTC are also made using the following exponential function (Pohl *et al.*, 2020b):

$$c(z) = \exp\left(\frac{z - l_1}{l_2}\right) l_3 \tag{8}$$

where z is the elevation above the bed surface and l_1 to l_3 are empirical fitting coefficients. Corresponding depth-averaged concentrations $\overline{c}$ are also determined over the whole turbidity current thickness (i.e. between $z = 0$ and $z = h_{\max}$).

Quantitative analysis of sedimentary deposits

Upon completion of each experimental run, the channel–basin facility is slowly drained to facilitate quantitative measurements of the sedimentary deposits produced by each HDTC. Raw images of the basin deposits (Fig. 3A) are reconstructed via a photogrammetry technique (Penna *et al.*, 2019). This method uses a Pentax K-70 DSLR camera (Pentax, Tokyo, Japan) and an 18 to 50 mm (f4–5.6) lens, capturing over 200 images of each deposit from a 360° field of view. Images are then processed via *Agisoft Photoscan* and aligned to one another via 48 fixed targets on the basin walls (Fig. 3A), with the central point for each target providing a geo-referenced position as Cartesian coordinates (x, y, z). The targets are calibrated using a Leica Disto (D110) laser distance measure (accuracy ±1.5 mm; Leica Microsystems, Wetzlar, Germany), with the origin (0, 0, 0) set in correspondence to the basin floor on the nearest right-hand corner (in the flow direction) of the facility (Fig. 1).

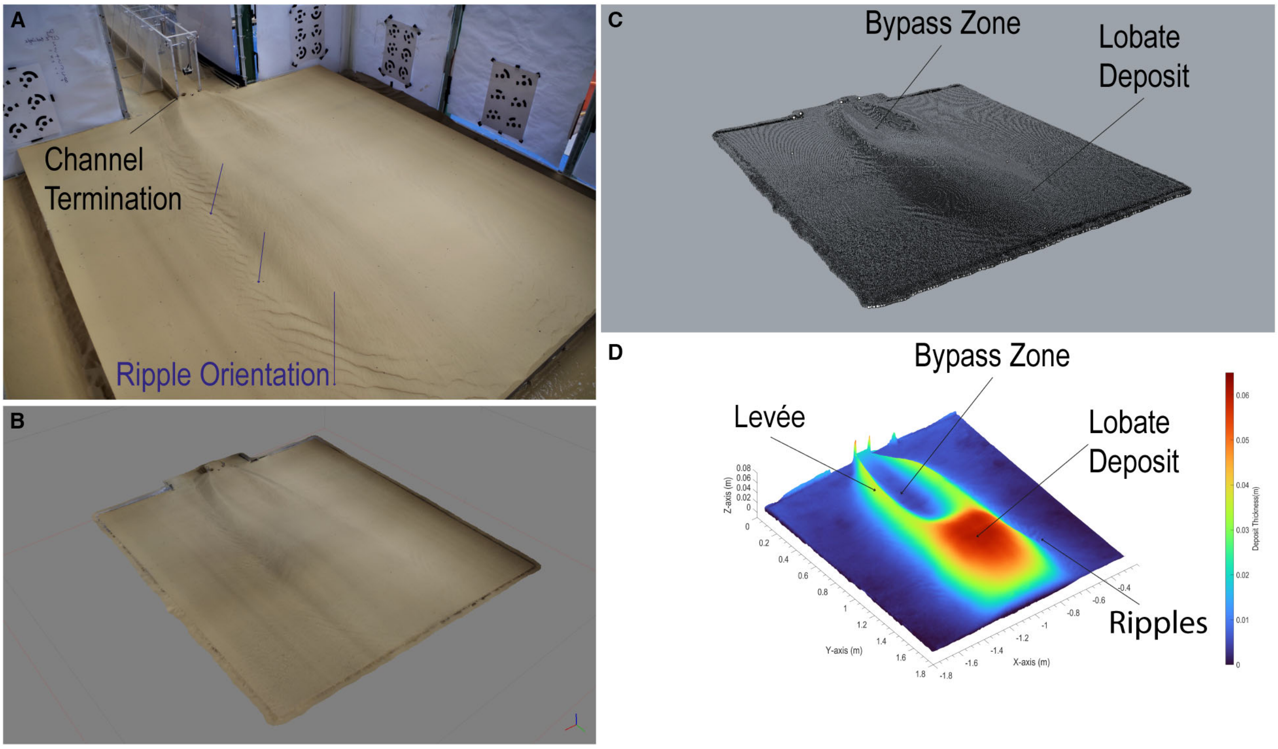

Fig. 3. Visual workflow for the photogrammetry methodology used to generate 3D basin deposit maps. (A) Photograph of deposit produced during run (Series S3, R3.2, Table 1), (B) scaled mesh of deposit produced from a high-density point cloud, (C) contoured mesh produced within *Rhinoceros 3D* and converted to a grid of Cartesian coordinates (X, Y, Z) at a 2 mm resolution, (D) spatial grid plotted via MATLAB to produce colourmaps of depositional thickness.

Once aligned and scaled, dense point clouds are converted into triangular meshes (Fig. 3B) and subsequently into structured grids (Fig. 3C) using the *Rhinoceros 3D* software (McNeel *et al.*, 2010). Each structured grid is then analysed using MATLAB to produce 3D contours and basin deposit maps (Fig. 3D). By contrast, the deposit thicknesses within the confined sloping channel are measured manually with a scale at along-channel increments of 0.10 m between the inlet manifold and the location of the SB-LOC.

Within the current study, each experimentally generated HDTC and its resulting channel and basin deposits are considered in isolation as individual events. However, they are likely to better represent a more protracted phase of sediment delivery into a deep-water depositional system, as has been considered in other experimental studies (e.g. De Leeuw *et al.*, 2016, 2018; Pohl *et al.*, 2019; Ferguson *et al.*, 2020). The purpose of physical experiments is therefore not to attempt to replicate natural system depositional architecture directly but, instead, to provide a reference to the underlying physical conditions which form individual elements within these depositional systems. On this basis, cored samples are taken from the basin deposit centreline at 0.10 m intervals from 0.90 to 1.60 m downstream of the SB-LOC location (i.e. 4.10–4.90 m downstream of the inlet), while another set of cores is taken at 0.10 m intervals in the lateral direction at the location of maximum deposit width [for Series S1, run R1.3 ($c_0 = 16\%$, 9° slope), Table 1]. Samples are prepared for size analysis by removing the upper 5 to 10 mm of the sediment sample to ensure the analysis is representative of the depositional conditions from the body of each HDTC (Bell *et al.*, 2021). Measurements of grain-size distributions from core samples are obtained using the laser particle size analyser and GRADISTAT (Blott & Pye, 2001) to assess the spatial variation of grading with reference to the initial sediment size distribution.

EXPERIMENTAL RESULTS

Turbidity current evolution between channel and basin

Initially, the controlled experimental inlet manifold and defined source conditions (Table 1) generate a well-developed, highly turbulent head region within the confined sloping channel. Immediately following this is a quasi-steady body region that remains stable and confined within the channel for the remaining duration of the test (Fig. 4A). On passing the SB-LOC location, the head (Fig. 4B) and body (Fig. 4C) of HDTCs spread radially and symmetrically into the horizontal basin, with lobe and cleft instabilities forming along the radially expanding and propagating front of all HDTCs (Fig. 4D). The head of the HDTCs also increases in height (i.e. due to billowing) during this radial expansion away from the SB-LOC (Fig. 4D and E), while the subsequent body of each HDTC reduces significantly in thickness (i.e. thinning body) immediately downstream of the SB-LOC region (Fig. 4C and F). The termination of the inflow conditions in each run causes the bodies of the HDTCs to diminish rapidly as any remaining residual momentum dissipates, resulting in a rapid reduction in current velocity and the mass deposition of the remaining suspended sediment from the current.

Representative time-averaged streamwise velocity profiles obtained from the body region of HDTCs (Fig. 5A) demonstrate that increases in the volumetric sediment concentration introduced at the source (i.e. $c_0 = 12\% \rightarrow 18\%$ for runs R1.1 → R1.4, Table 1) results in an increase in the maximum velocities $U_{\max}$ of the HDTCs at all UVP measurement locations. These velocity profiles show that the elevation $H_{\max}$ at which the maximum velocity $U_{\max}$ occurs within the HDTCs, relative to the bed, is at its highest when HDTCs are confined within the channel, prior to encountering the SB-LOC. Once downstream of the SB-LOC, this height $H_{\max}$ initially reduces, as observed at UVP 3, before increasing again upon reaching UVP 4 (Fig. 5A). The HDTCs are also observed to achieve their largest velocities (i.e. highest $U_{\max}$ values) downstream of the SB-LOC between UVP 2 and UVP 3 (Fig. 5A), after which they begin to decelerate, as observed at UVP 4. The overall height or thickness $h_{\max}$ of the individual HDTCs (see *Flow scaling and characterization* section) are measured directly from the time-averaged UVP velocity profiles (Fig. 5A). These show that the height of each individual HDTC remains approximately constant in the confined channel between UVP1 and UVP2 (i.e. varying between $h_{\max} = 0.074$–0.113 m and 0.074–0.092 m at UVP1 and UVP2, respectively, Fig. 5A). By contrast, measurements of $h_{\max}$ at UVP 3 and UVP 4 show that, once downstream of the SB-LOC, the overall thickness of the HDTCs is significantly reduced (i.e. $h_{\max} = 0.056$–0.068 m and 0.041–0.050 m, respectively). Figure 5B compares the representative time-averaged velocity profiles for experimental runs

Fig. 4. (A) Formation of the high-density turbidity current (HDTC) head and quasi-steady body region along the confined, sloping channel with flow direction being from left to right, (B) symmetrical radial expansion of the HDTC head downstream of the SB-LOC, (C) expansion of the HDTC body region downstream of the SB-LOC, (D) side on view of the HDTC head expansion 0.25 s after exiting the SB-LOC, (E) side on view of the radially-expanding HDTC, 2.5 s after exiting the SB-LOC, (F) side on view of HDTC body collapse downstream of the SB-LOC. (note the absence of an internal hydraulic jump immediately downstream of the SB-LOC).

with a fixed input volumetric sediment concentration of 18% with varying channel slope angles from 9°, to 6° and 3° (i.e. R1.4, R2.4 and R3.2, see Table 1). The systematic reduction in slope angle between the three runs results in a reduction of the maximum velocity $U_{\max}$ achieved by HDTCs at UVP 3, from $U_{\max} = 1.23 \text{ m s}^{-1}$ (for a 9° slope break) to $U_{\max} = 0.96 \text{ m s}^{-1}$ (for a 3° slope break). A similar trend is also observed at the other UVP locations.

Sediment samples were syphoned at different elevations within the individual HDTCs to measure the suspended sediment concentration profile immediately downstream of the SB-LOC (see Fig. 6 and Appendix S1). These measurements indicate a general exponential decrease in concentrations with increasing elevation within the HDTCs, as expected (Eq. 8). The suspended sediment profiles also indicate a systematic reduction in measured concentrations at all elevations as the initial volumetric concentration of sediment introduced at the source is reduced (i.e. $c_0 = 18\% \rightarrow 12\%$, Fig. 6A). Furthermore, there appears to be some evidence of a marginal

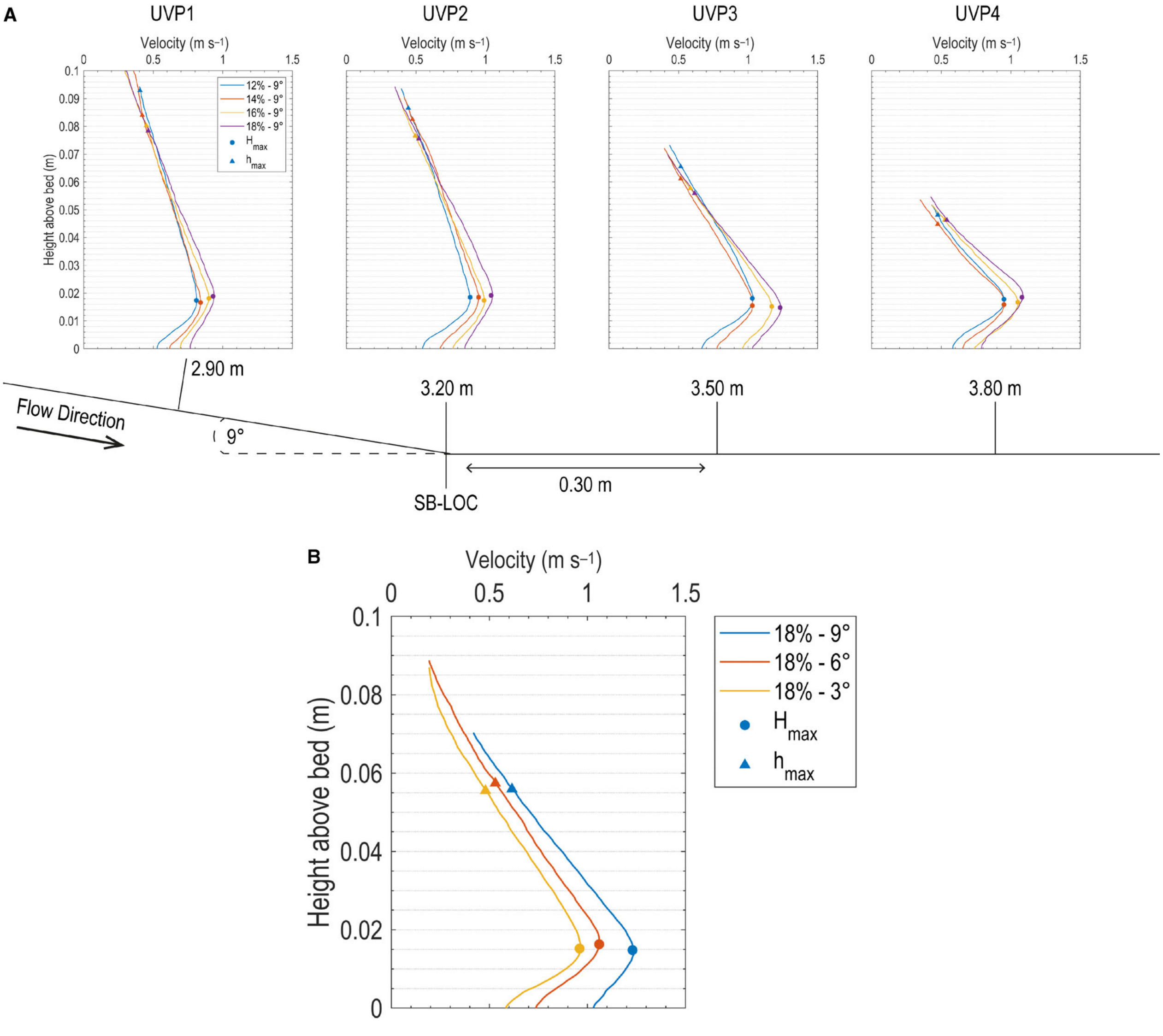

Fig. 5. (A) Time-averaged velocity profiles of high-density turbidity currents (HDTCs) at UVP 1–UVP 4 locations, showing the effect of increasing the initial volumetric concentration of suspended sediment c_0 (i.e. 12% → 18%) for runs with a fixed 9° channel slope angle (Series S1, Table 1). (B) Time-averaged velocity profiles of HDTCs at UVP 3 (i.e. 0.3 m downstream of SB-LOC), showing the effect of a channel slope reduction (i.e. 9° → 3°) for runs with a fixed initial volumetric sediment concentration of 18%.

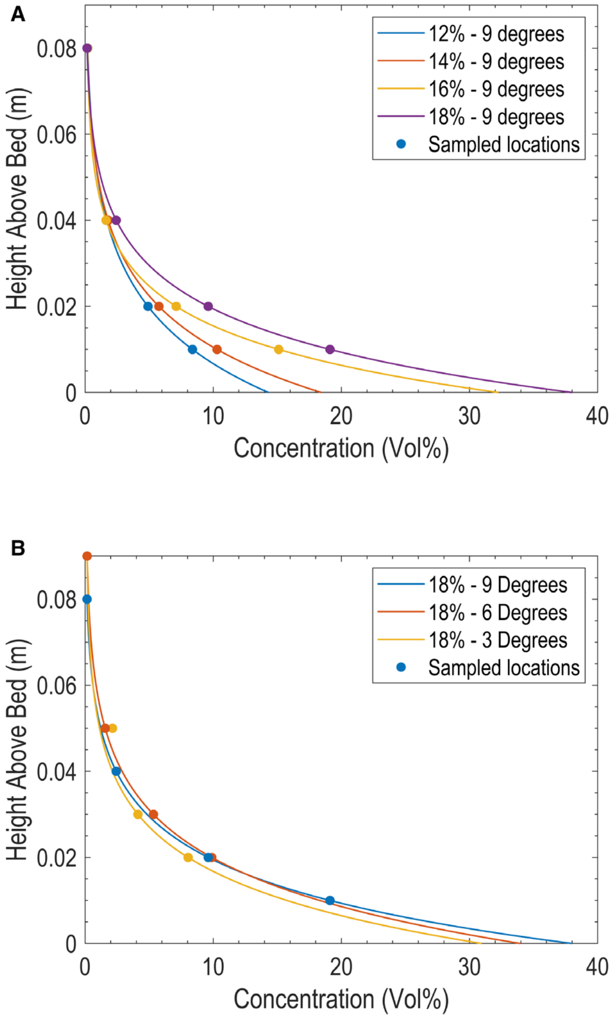

Fig. 6. (A) Suspended sediment concentration profiles for high-density turbidity current (HDTCs) sampled immediately downstream of the SB-LOC, showing the effect of increasing initial volumetric concentration of suspended sediment c_0 (i.e. 12% → 18%) for runs with a fixed 9° channel slope angle (Series S1, Table 1). (B) Suspended sediment concentration profiles, showing effect of a channel slope reduction (i.e. 9° → 3°) for runs with a fixed initial volumetric sediment concentration of 18%. Solid lines show the best fit of concentration measurements to exponential fitting function (Eq. 8).

reduction in the suspended sediment concentrations (for a given source volumetric concentration) as the channel slope angle is reduced from 9° to 3° (Fig. 6B), potentially due to increased sediment bypass on steeper channel slopes. Depth-averaged volumetric concentrations $\overline{c}$ measured over the full thickness of individual HDTC runs range between 4.0 to 9.4%, 4.0 to 9.5% and 3.9 to 8.3% for S1 (i.e. channel slope = 9°, Fig. 6A), S2 (6°) and S3 (3°) runs, respectively. Corresponding depth-averaged basal layer concentrations $\overline{c}_b$, calculated by the exponential fitting function (Eq. 8) between the bed surface and elevation of the velocity maximum $U_{\max}$ within each TC, range between 9.2% to 23.6%, 8.4% to 21.7% and 9.2% to 19.6% for S1 (9°), S2 (6°) and S3 (3°) runs, respectively.

The prevailing flow characteristics of the HDTCs are illustrated by the downstream variations of the shear velocity U_* (Eq. 3) (Fig. 7A and B). These plots indicate that, for the HDTC run out from the confined channel into the unconfined basin for a fixed slope break angle at the SB-LOC (for example, 9°, Fig. 7A), the shear velocities at all UVP locations increase with increasing initial volumetric concentrations of suspended sediment (i.e. $c_0 = 12\% \rightarrow 18\%$). Shear velocities are also observed to increase consistently between UVP 1 (i.e. within the confined channel) and UVP 3 (i.e. in the unconfined basin, downstream of the SB-LOC), where it reaches a maximum value (U_* = 0.059–0.074 m s^{-1}, Fig. 7A) before decreasing again at UVP 4 (U_* = 0.055–0.062 m s^{-1}, Fig. 7A). In addition, for HDTCs that have the same initial volumetric concentration of suspended sediment (for example, $c_0 = 18\%$, Fig. 7B), a reduction in the channel slope break angle generally leads to a reduction in the shear velocity U_*, particularly in the unconfined basin. This plot also shows the same general increasing trend in U_* between UVP 1 and UVP 3, followed by a reduction at UVP 4, as before. Overall, the range of shear velocity values measured at each slope break condition range between U_* = 0.050 to 0.074 m s^{-1} (i.e. channel slope = 9°); 0.049 to 0.066 m s^{-1} (i.e. slope = 6°); and 0.057 to 0.0629 m s^{-1} (i.e. slope = 3°) (see Appendix S1 for additional U_* plots).

Variations in the densimetric Froude numbers Fr_D from the same representative HDTCs as considered in Fig. 7A (i.e. c_0 = 12–18%, channel slope = 9°) indicate that their flow regimes remain supercritical (i.e. $\mathrm{Fr}_D > 1$) throughout the transition between the confined channel and basin floor (Fig. 7C). Indeed, Fr_D values are shown to increase with downstream distance between UVP 1 and UVP 3 (i.e. Fr_D = 2.15–2.55 and Fr_D = 3.3–3.8, respectively), before levelling off or even reducing slightly at UVP 4 (i.e. $\mathrm{Fr}_D = \mathrm{Fr}_D$ = 3.2–4.1). In general, the magnitude of Fr_D values also have an inverse relationship with the initial concentration of suspended sediment c_0, with lower initial concentrations (i.e. c_0 = 12%) typically resulting in HDTCs with the highest densimetric Froude numbers (see Fig. 7C). By contrast, reducing the

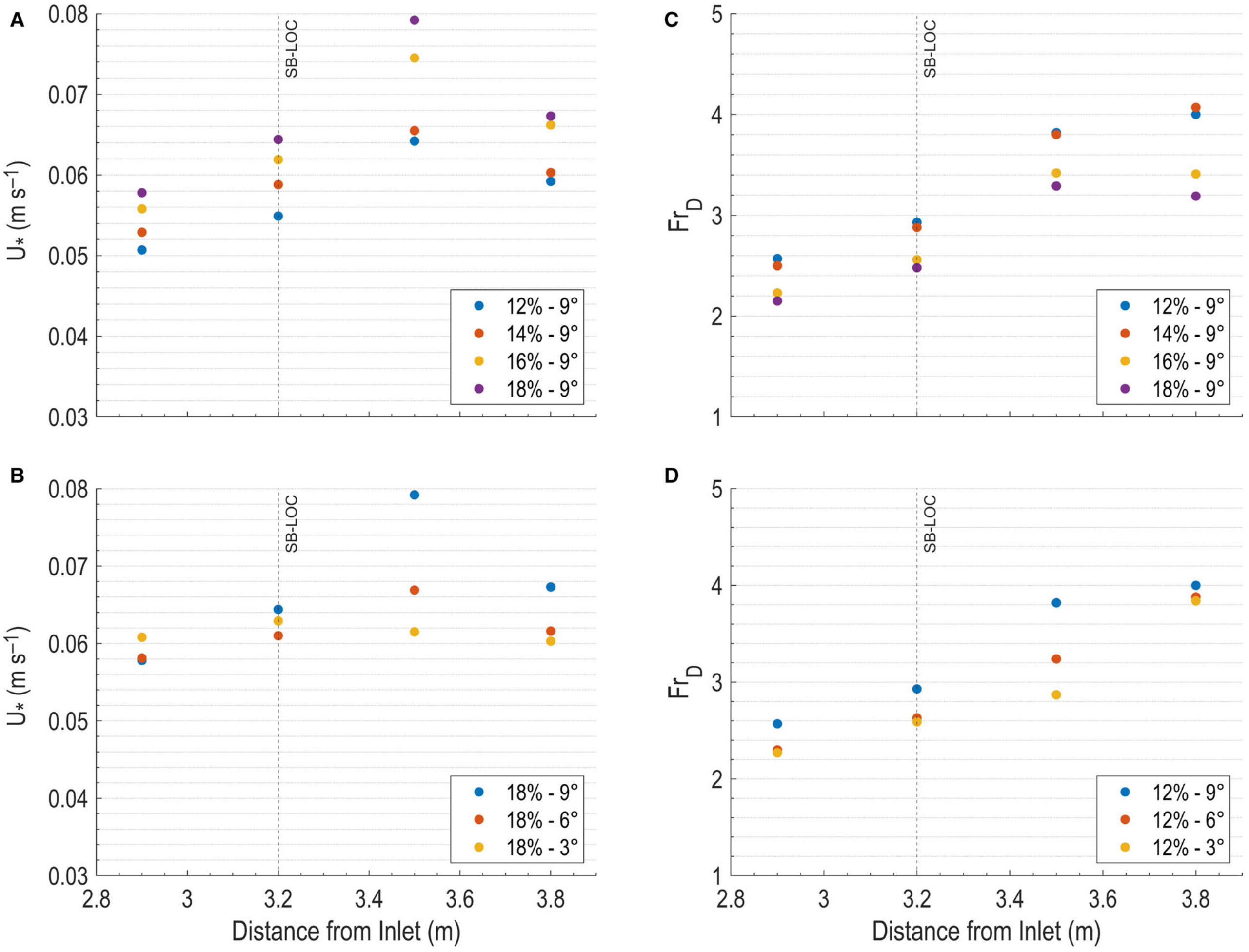

Fig. 7. Downstream variations in the shear velocity U_* (plots A and B) and densimetric Froude number Fr_D (plots C and D) between UVP 1 to UVP 4 locations showing (i) the effect of varying initial volumetric sediment concentration c_0 for runs with a fixed 9° channel slope angle (plots A and C), and (ii) the effect of varying channel slope angle for runs with a fixed initial volumetric sediment concentration of 18% (plots B and D).

channel slope angle from 9° to 3° (i.e. for fixed $c_0 = 12\%$, Fig. 7D) slightly reduces the Fr_D values at all measurement locations (UVP 1 → UVP 4). However, the flow regime of the HDTCs remains supercritical throughout the channel–basin transition, again typically increasing with downstream distance from the inlet (i.e. from $\mathrm{Fr}_D = 2.15$–2.6 at UVP 1 to $\mathrm{Fr}_D = 3.85$–4.0 at UVP 4).

Calculation of the Rouse number ζ for the D_{10}, D_{50} and D_{90} percentiles of the input sediment grain-size distribution (Fig. 8) indicate that all ζ values for the D_{50} and D_{10} percentiles lie in the washload regime (i.e. $\zeta < 0.8$) throughout the channel basin transition. By contrast, the equivalent ζ values for the coarse D_{90} percentile lie either in the 100% or 50% suspended load regime (i.e. $\zeta = 0.8$–1.2 or $\zeta = 1.2$–2.5, respectively) (Fig. 8). Furthermore, Fig. 8A indicates that, at a fixed channel slope break (i.e. 9°), the HDTCs generated under the lowest initial volumetric sediment concentration (i.e. $c_0 = 12\%$) have the highest Rouse numbers ζ, and vice versa. This plot also shows that, as the HDTCs transition between the channel and basin (i.e. UVP 1 → UVP 3), the ζ values decrease with increasing distance from the inlet, suggesting that HDTCs become more efficient in transporting their sediment loads in suspension. Similarly, the increase in ζ values at UVP 4 indicates a reduction in the efficiency for suspended load transport further into the basin, particularly for larger grain-size percentiles. Reducing the slope break angle (i.e. for fixed $c_0 = 12\%$, Fig. 8B) has an inconsistent effect on ζ values

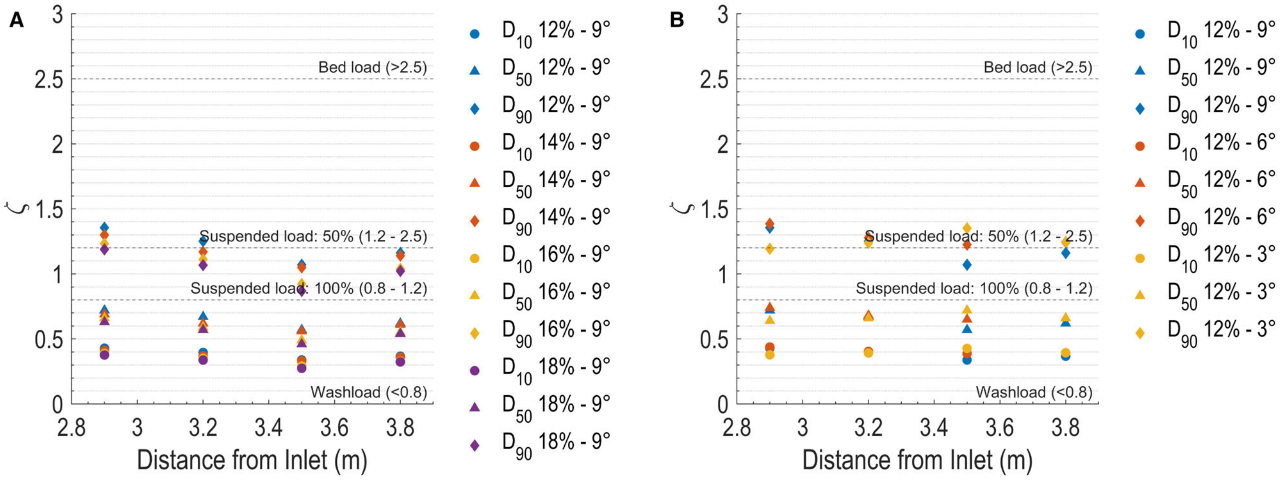

Fig. 8. Downstream variations in the Rouse parameter (ζ) between UVP 1–UVP 4 locations for $D_{10} : D_{50} : D_{90}$ size classes, showing (A) the effect of varying initial volumetric sediment concentration c_0 (i.e. 12%–18%) for runs conducted at a channel slope of 9°, and (B) the effect of varying channel slope angle (i.e. 9°–3°) for runs conducted with an initial volumetric sediment concentration of 12%.

within the confined channel (i.e. UVP 1 → UVP 2), but leads to an overall increase in ζ values within the unconfined basin. In this case, the ζ values for the coarse D_{90} percentile largely reside in the 50% suspended load transport regime (i.e. $\zeta = 1.2$–2.5, Fig. 8B).

The kinetic energy E_k (Eq. 6) and potential energy E_p (Eq. 7) for the same representative HDTCs (as considered previously) are both shown to increase at all UVP locations as the initial volumetric concentration of suspended sediment c_0 increases (i.e. $c_0 = 12\% \rightarrow 18\%$ for channel slope = 9°, Fig. 9A and 9C). In each of these runs, there is a consistent downstream increase in E_k values from UVP 1 to the maximum E_k value at UVP 3 (i.e. 0.30 m downstream of the SB-LOC). Further downstream at UVP 4 (i.e. 0.6 m from the SB-LOC), the corresponding E_k values indicate a significant reduction, but remain higher than E_k at UVP 2 (i.e. at the SB-LOC). In contrast, the potential energy E_p decreases consistently in the downstream direction from UVP 1 and UVP 4, with a more pronounced reduction occurring as the HDTCs pass downstream of the SB-LOC (i.e. between UVP 2 and UVP 3, Fig. 9C). Reducing the channel slope angle from 9° to 3° results in a reduction in E_k at all UVP positions (Fig. 9B). This also diminishes the downstream variability in E_k values between UVP1 and UVP 4, which remain largely unchanged through the channel–basin transition at this lower slope break angle (i.e. slope = 3°, $c_0 = 12\%$, Fig. 9B). In contrast, the reduction in the slope break angle is shown to have minimal effect on the potential energy E_p at each UVP position, or the general reduction in E_p values in the downstream direction (Fig. 9D).

Depositional trends

Deposition in sloping confined channel

Observations and direct measurements of the deposit thickness from the channelized HDTCs along the length of the sloping, confined channel are shown in Fig. 10 for the three bed slope angles (i.e. 9°, 6° and 3°) and the four initial suspended sediment concentrations c_0 (i.e. $c_0 = 12\%$, 14%, 16% and 18%) tested. All HDTCs deposit sediments within the channel, and results indicate that the deposit thickness increases as the channel slope decreases from 9° (Fig. 10A) to 3° (Fig. 10C). There is no observable bedform development on the surficial deposits along the channel length and the bed profiles remain smooth in all runs. In close proximity to the inlet manifold, the generated HDTCs produce a zone of scour due to the high inlet velocities (i.e. u_0, Table 1) and Reynolds numbers in this region. This initial scour length reduces as the channel slope angle reduces (i.e. slope = 9°–3°, Fig. 10A to C), as the high inflow velocities are sustained over a shorter downstream distances at lower slopes. At the largest channel slope angle of 9° (Fig. 10A), the majority of channel deposition from the HDTCs is observed to occur towards the end of the

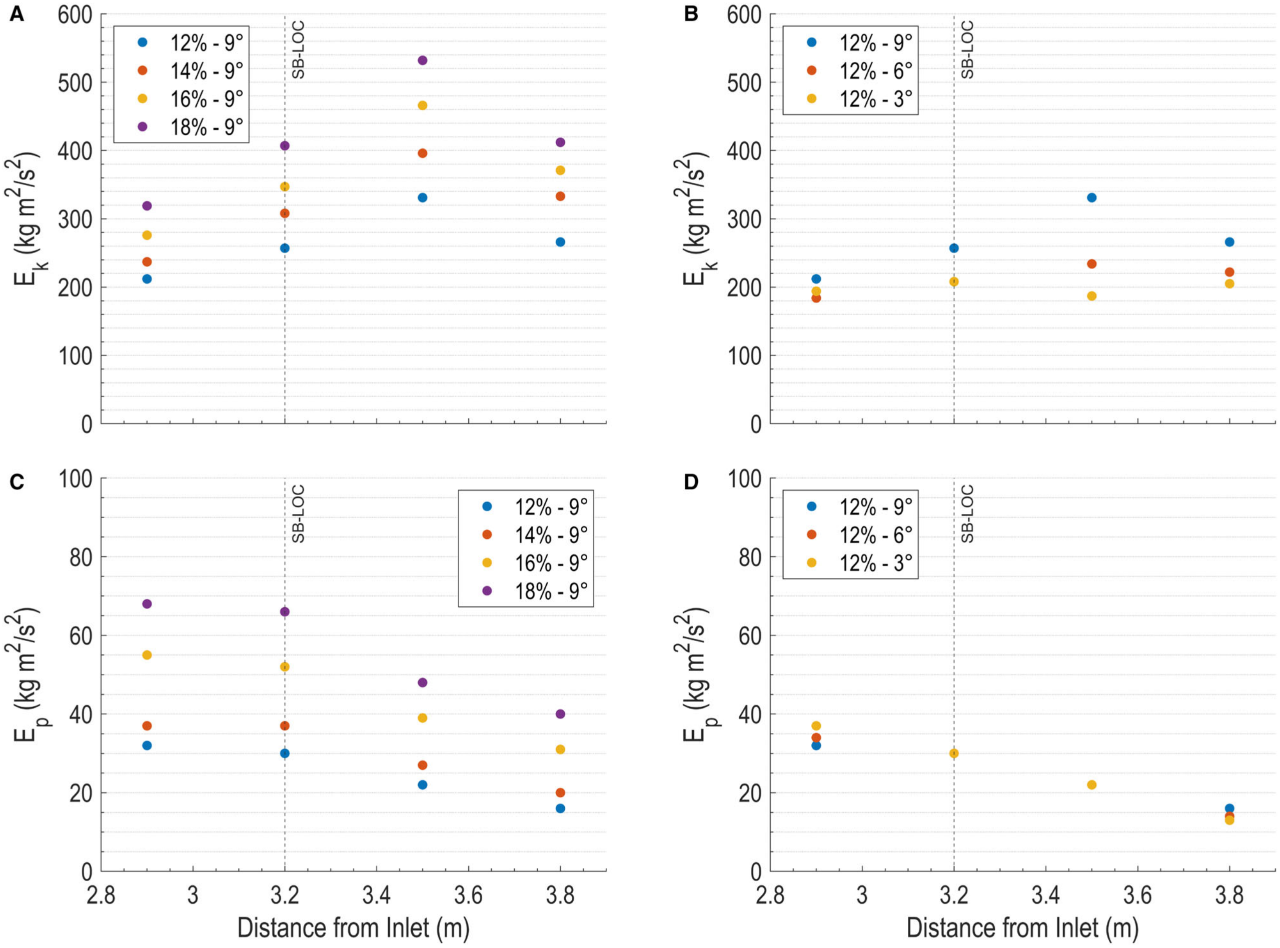

Fig. 9. Downstream variations in the calculated kinetic energy E_k (plots A and B) and potential energy E_p (plots C and D) between UVP 1–UVP 4 locations showing: (i) the effect of varying initial volumetric sediment concentration c_0 for runs with a fixed 9° channel slope angle (plots A and C), and (ii) the effect of varying channel slope angle for runs with a fixed initial volumetric sediment concentration of 12% (plots B and D).

discharge period, and the overall deposit thicknesses increase marginally as the initial suspended sediment concentrations of HDTCs decreases (i.e. c_0 = 18% → 12%, Fig. 10A). These channel deposits increase in thickness with increasing distance from the end of the scour region, with the maximum thickness between 1.5 cm (i.e. c_0 = 18%) and 2.7 cm (i.e. c_0 = 14%) occurring at the SB-LOC. The channel deposit for the HDTC generated with c_0 = 12% deviates from this trend, in that the maximum deposit thickness of 3.30 cm occurs 1.60 m downstream of the inlet (i.e. halfway along the channel between the inlet and the SB-LOC).

Reducing the channel slope angle to 6° and 3° results in the channel deposits (Figs. 10B and C) produced by HDTCs aggrading steadily over the 50 s duration of each test. Along-channel deposit profiles recorded at the slope angle of 6° (Fig. 11B) indicate maximum thicknesses between 6.8 cm (for c_0 = 18%) and 7.7 cm (for c_0 = 14%) at a distance of 1.3 m downstream of the inlet manifold. Lowering the slope to 3° further increases the overall channel deposit (Fig. 10C), with maximum thicknesses between 9.9 cm (for c_0 = 12%) and 10.1 cm (for c_0 = 18%), also recorded 1.30 m downstream of the inlet manifold.

The measured depositional profiles along the confined channel can also be used to estimate the overall volume of sediment deposited by the HDTCs within the channel. This can then be compared with the total sediment volume introduced into the channel–basin system via the inlet manifold, obtained from the initial volumetric sediment concentration c_0 and the flow rate data (see

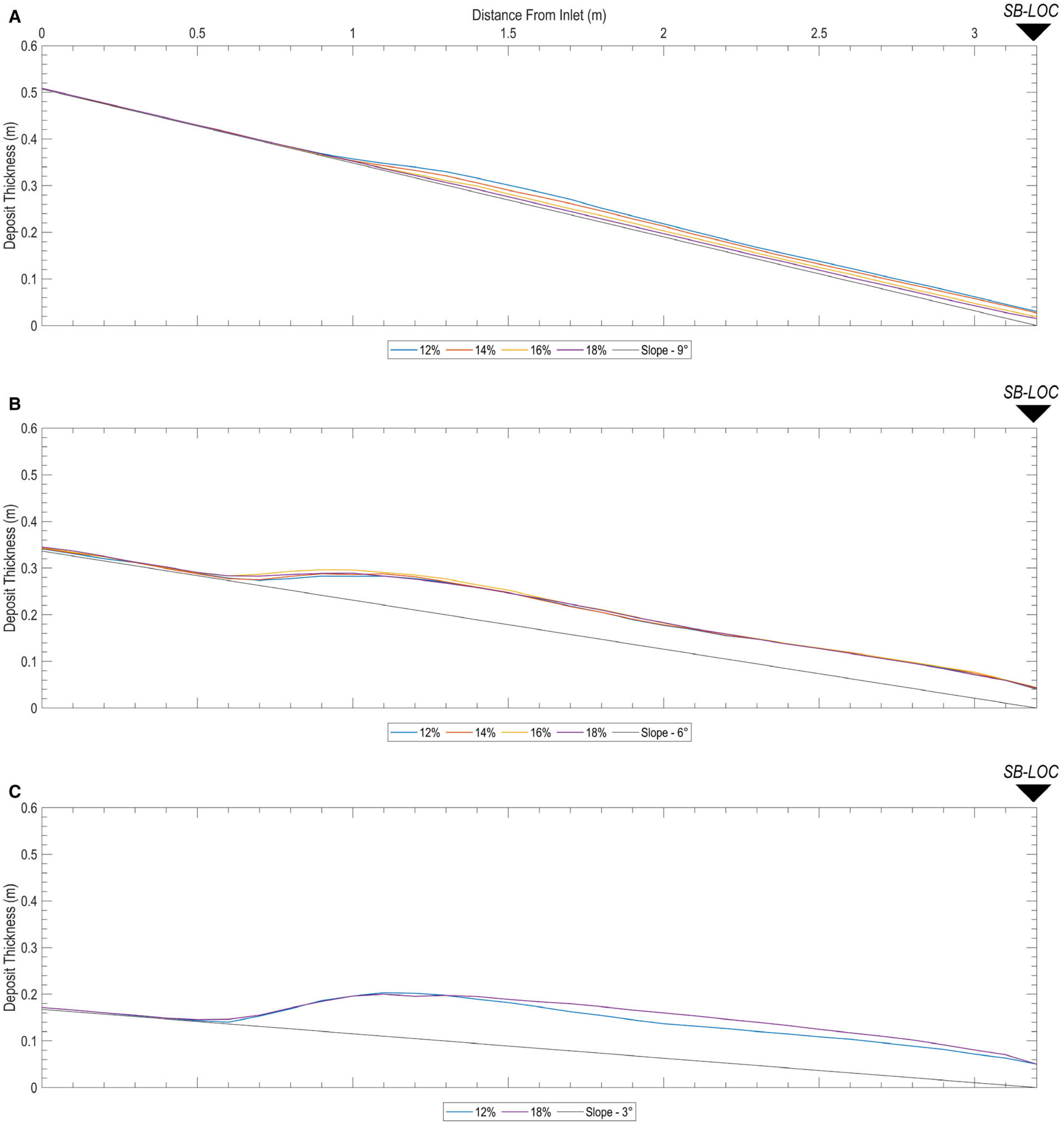

Fig. 10. Bed deposit profiles within the sloping, confined channel for (A) series S1 (i.e. channel slope = 9°; c_0 = 12–18%, Table 1), (B) series S2 (i.e. slope = 6°, c_0 = 12%–18%, Table 1), and (C) series S3 (i.e. slope = 3°, c_0 = 12% and 18%, Table 1).

Appendix S1). This provides a means of estimating how much of the initial sediment volume discharged during each HDTC bypasses the confined channel slope and is therefore deposited in the unconfined basin. For the channel slope angle of 9°, the overall volumes of sediment deposited in the channel decrease (i.e. 20% → 13.8% → 7.5% → 4.2%) as the initial volumetric concentration of suspended sediment increases (i.e. c_0 = 12% → 14% → 16% → 18%). Lowering the channel slope angle from 9° to 6° also results in an increase in the proportion of the discharged

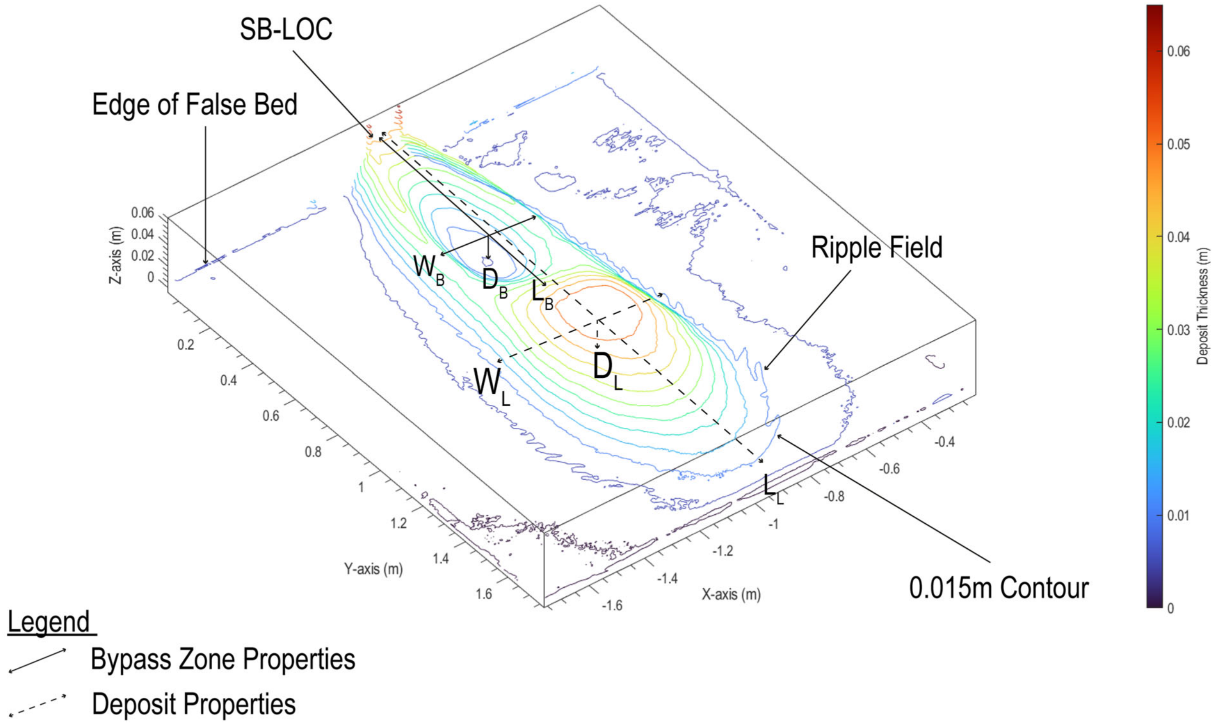

Fig. 11. Example contour plot showing a typical depositional feature in the basin downstream of the SB-LOC, indicating key deposit geometrical parameters of the sediment bypass region (L_B, W_B, D_B) and the subsequent lobe deposit (L_L, W_L, D_L).

sediment input that is deposited within the channel ranging between 44.5% → 31.2% (for c_0 = 12% → 18%). A further reduction in the channel slope from 6° to 3° again increases the volume of channel deposited sediment, with the proportion of the total sediment input ranging between 52.5% → 43% (for c_0 = 12% → 18%).

Deposition in horizontal unconfined basin

Upon exiting the channel at the SB-LOC, all HDTCs form two flanking levées that have a convex geometry and extend out into the basin from the channel edges (Fig. 3D). These levées flank a central low deposition region formed by the body region of each HDTC, representing the sediment bypass zone immediately downstream of the SB-LOC. Further into the basin, sedimentation from all HDTCs forms lobate geometries. These depositional features increase abruptly in thickness along the basin centreline and downstream of the sediment bypass zone. Flanking all lobate bodies is a thin sediment fringe dominated by current ripples (Fig. 3A).

The geometries of the basin sediment bypass zones and lobate deposits produced by HDTCs are analysed in terms of their geometrical lengths, widths, and the maximum bypass zone depths and lobe deposit thicknesses (Fig. 11). The length L_L and width W_L of a lobate deposit are measured with reference to the z = 0.015 m contour, whilst maximum thickness D_L is based upon subtracting the deposit profile generated by the photogrammetry technique (see *Quantitative analysis of sedimentary deposits* section) from the initial basin bed condition. Similarly, the length L_B, width W_B and depth D_B of the sediment bypass zone are measured with reference to the flanking crest elevation of the levée and the bed thickness at the lowest point in the bypass zone (Fig. 11).

Colour-coded 3D basin deposit maps (Fig. 12) indicate that the plan-form spatial extent and thickness or depth of each lobate body (L_L, W_L, D_L) and bypass zone (L_B, W_B, D_B) are dependent on the slope angle and initial suspended sediment concentration c_0. The geometrical dimensions of these lobes and bypass regions, along with the lobe centroid positions (i.e. the downstream distance of the maximum deposit thickness from the SB-LOC), are detailed for each

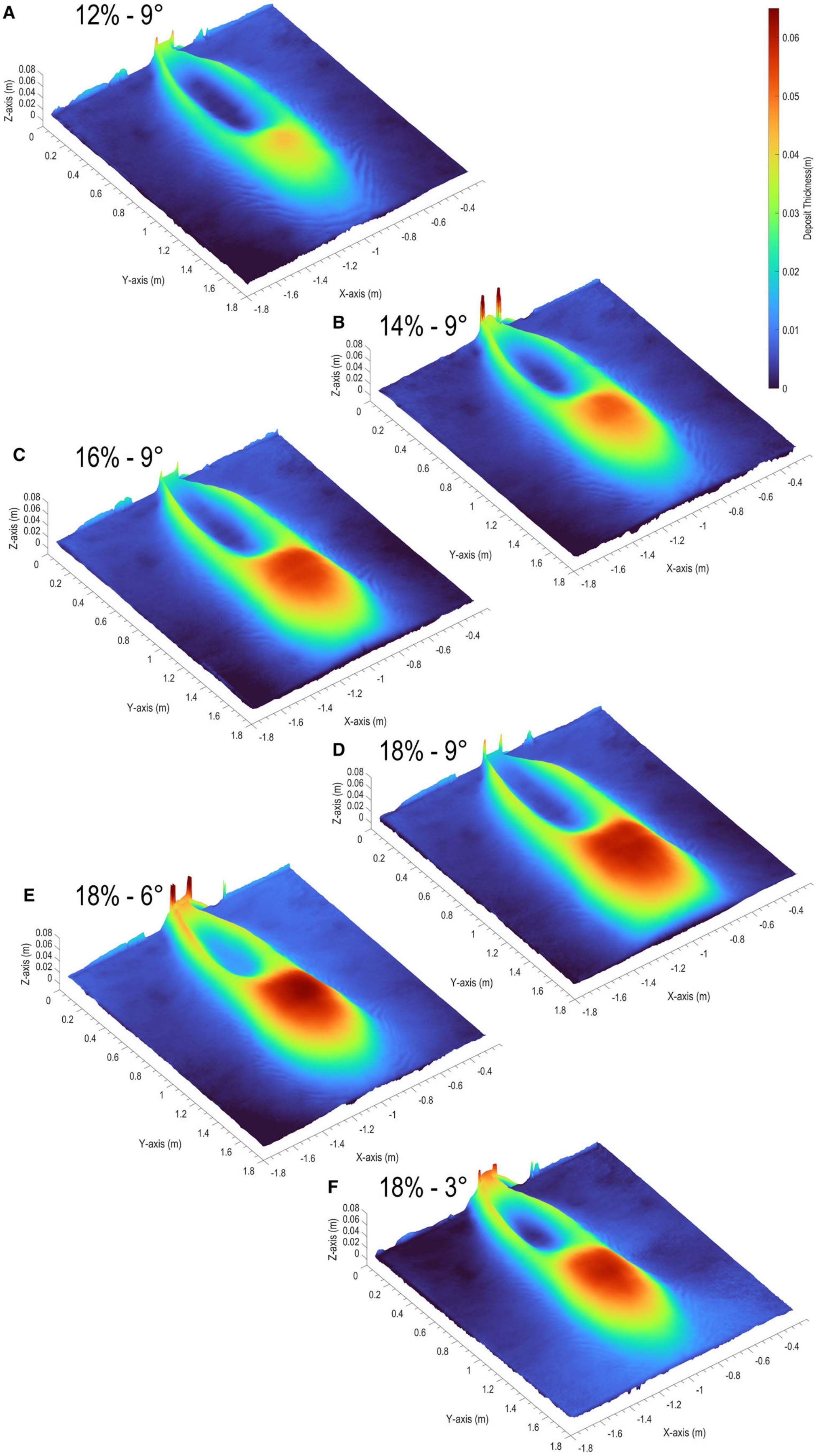
A
12% - 9°
B
14% - 9°
C
16% - 9°
D
18% - 9°
E
18% - 6°
F
18% - 3°
Z-axis (m)
0.08
0.06
0.04
0.02
0
Y-axis (m)
0
0.2
0.4
0.6
0.8
1
1.2
1.4
1.6
1.8
X-axis (m)
-1.8
-1.6
-1.4
-1.2
-1
-0.8
-0.6
-0.4
Deposit Thickness(m)
0.06
0.05
0.04
0.03
0.02
0.01
0

Fig. 12. Three-dimensional deposition colourmaps for selected runs (A) c_0 = 12%; slope = 9°, (B) c_0 = 14%; slope = 9°, (C) c_0 = 16%; slope = 9°, (D) c_0 = 18%; slope = 9°, (E) c_0 = 18%; slope = 6°, and (F) c_0 = 18%; slope = 3° (see Table 1 for details). Deposit thicknesses are shown to highlight the sediment bypass region, flanked by two convex depositional features, and the downstream depositional lobe element.

experimental run in Table 2. Basin lobe deposits for the same representative runs as considered previously (i.e. slope = 9°, c_0 = 12–18%, Fig. 12A to D) show that when the initial volumetric sediment concentration c_0 is increased, the resulting HDTCs produce lobate deposits that are longer, wider and thicker. The downstream location of the lobate deposit centroid also increases from 1.07 m → 1.26 m (for c_0 = 12% → 18%). Non-dimensional aspect ratios L_L/W_L and L_L/D_L for these lobate deposits are found to decrease as c_0 is increased between runs (for example, L_L/W_L = 2.92 → 2.39 and L_L/D_L = 37.17 → 27.96 for c_0 = 12% → 12%, Table 2). Reducing the channel slope break angle (i.e. 9° → 3°) between runs with a fixed c_0 value (for example, c_0 = 18%) has a less consistent influence of the lobate deposit aspect ratios L_L/W_L : L_L/D_L, which vary from 2.39 : 27.96 (at 9° slope); 2.70 : 25.75 (at 6° slope, see Fig. 12E) and 2.91 : 28.16 (at 3° slope, Fig. 12F). Corresponding distances downstream of the SB-LOC at which the lobate deposit centroid occurs also typically reduce (i.e. shift towards the SB-LOC) as the channel slope break angle is reduced (see Table 2).

The geometric dimensions of the sediment bypass zones (i.e. L_B, W_B and D_B, Fig. 11) produced by HDTCs immediately downstream of the SB-LOC are shown to decrease in length L_B, while increasing in both width W_B and depth D_B (Table 2), as the initial sediment concentration c_0 is increased between runs. Values of the bypass aspect ratio L_B/W_B therefore decrease as c_0 is increased, such that L_B/W_B = 2.80 → 2.36 (for c_0 = 12% → 18% runs at 9° slope); 3.37 → 2.33 (c_0 = 12% → 18% at 6° slope) and 2.51 → 2.06 (c_0 = 12% → 18% at 3° slope) (see Table 2). Ratios of L_B/D_B also generally decrease as c_0 is increased, although this reduction is most apparent between c_0 = 12% → 14% under each channel slope break condition, with L_B/D_B = 42.0 → 30.8 (for 9° slope) and 54.0 → 31.3 (for 6° slope). At the lowest slope break angle of 3°, L_B/D_B = 52.0 → 25.4 (for c_0 = 12% → 18%). Indeed, the reduction in slope break angle has the overall effect of decreasing L_B, W_B and D_B values in the bypass zones (Table 2). However, the corresponding aspect ratios L_B/W_B and L_B/D_B show no general trend with these changing slope break conditions (for runs with fixed c_0 values).

Deposit grain-size trends

It is also informative to consider the nature of any spatial variability in the grain-size distributions within the basin lobate deposits. As such, cores taken along the centreline axis of lobate deposits (A–A^1, Fig. 13A) and across a perpendicular transect at the point of maximum width W_L (B–B^1, Fig. 13A). Figure 13B shows the measured grain-size distributions along A–A^1, for run R1.3 (i.e. slope = 9°, c_0 = 16%, Table 1), indicating that the lobe deposit has a general fining in the downstream direction (A → A^1). The corresponding percentile grain sizes (D_{10} : D_{50} : D_{90}) along the A–A^1 axis decrease from 133 : 229 : 400 μm at 0.90 m to 121: 198: 326 μm at 1.6 m (i.e. downstream distances from the SB-LOC). Figure 13C shows the corresponding grain-size distributions across the lateral deposit axis B–B^1, with symmetrical fining from the centreline to the margins of the lobe deposit. Corresponding D_{10} : D_{50} : D_{90} values across this B–B^1 transect decrease from 138 : 226 : 365 μm at the lobate centreline (i.e. intersect with A–A^1) to an average of 109 : 188 : 311 μm at the lobe margins. Similar grain-size distributions measured in other experimental runs with different channel slope break angles and/or initial volumetric sediment concentrations display similar along-lobe and cross-lobe fining trends to those described above (see Appendix S1).

DISCUSSION

Flow properties of confined and unconfined high density turbidity currents

Combining the measurements of HDTC velocity and concentration profiles from all runs demonstrates that an increase in the initial volumetric sediment concentration c_0 increases both the maximum velocities throughout the channel–basin system (Fig. 5) and the measured volumetric concentrations (Fig. 6). Furthermore,

Table 2. Geometrical dimensions and aspect ratios of the sediment bypass regions (or channel–lobe transition zones – CLTZs) and basin lobe elements produced downstream of the SB-LOC within Series S1–S3 runs (see Table 1).

Experimental parameters			Bypass zone dimensions					Lobate deposit dimensions							
Run	Initial conc. C_0 (%)	Slope angle (°)	Length L_B (m)	Width W_B (m)	Depth D_B (m)	L_B/W_B	L_B/D_B	Deposit length L_L (m)	Deposit width W_L (m)	Deposit thickness D_L (m)	Dist. to max width from SB-LOC (m)	Centroid position from SB-LOC (m)	L_L/W_L	W_L/D_L	L_L/D_L
R1.1	12	9	0.84	0.30	0.02	2.80	42.00	1.58	0.54	0.042	0.88	1.07	2.92	12.85	37.17
R1.2	14	9	0.77	0.32	0.025	2.40	30.80	1.66	0.57	0.049	1.00	1.09	2.91	11.63	33.33
R1.3	16	9	0.82	0.33	0.029	2.48	28.27	1.69	0.63	0.057	1.31	1.09	2.68	11.05	29.59
R1.4	18	9	0.86	0.36	0.030	2.36	28.66	1.70	0.71	0.060	1.34	1.26	2.39	11.83	27.96
R2.1	12	6	0.81	0.24	0.015	3.37	54.00	1.45	0.48	0.036	0.93	1.02	3.02	13.33	40.27
R2.2	14	6	0.75	0.25	0.024	3.00	31.25	1.55	0.49	0.045	1.07	1.02	3.16	10.88	34.44
R2.3	16	6	0.68	0.26	0.019	2.61	35.78	1.58	0.54	0.054	1.12	1.05	2.92	10.00	29.25
R2.4	18	6	0.70	0.30	0.021	2.33	33.33	1.65	0.61	0.064	1.20	1.07	2.70	9.53	25.75
R3.1	12	3	0.78	0.31	0.015	2.51	52.00	1.42	0.45	0.035	0.80	0.97	3.15	12.85	40.57
R3.2	18	3	0.66	0.32	0.026	2.06	25.38	1.69	0.58	0.060	1.15	1.09	2.91	9.66	28.16

increasing the c_0 value also reduces the overall flow thickness of the HDTCs and, specifically, the vertical elevation $h_{\max}$ within the current at which velocity $U = 0.5U_{\max}$ (Fig. 5A). Similarly, a reduction in the channel slope break angle from 9° to 3° results in reduced flow velocities for HDTCs generated under equivalent initial volumetric sediment concentrations c_0 (Fig. 5B), as well as marginally reduced suspended sediment concentrations (Fig. 6B) downstream of the SB-LOC. As such, the flow dynamics of the confined and unconfined HDTCs appear to be largely driven by two physical mechanisms. Firstly, for the range of initial volumetric sediment concentrations tested in the study (i.e. $c_0 = 12$–18%), the currents generated from higher c_0 values generally achieve higher flow velocities at all UVP positions in the channel and basin (Fig. 5A) for any channel slope break condition. This is primarily due to increased suspended sediment concentrations within the turbidity currents (for example, Fig. 6A) and, hence, the larger excess densities driving the flows. It is acknowledged here, however, that further increase in the initial sediment concentration c_0 may reach a point where the turbidity currents can no longer maintain this additional sediment load in suspension (i.e. when the transport carrying capacity of the current is reached), and the excess sediment load will be deposited within the confined channel. Secondly, higher channel slope break angles also increase the volume of the released sediment that bypasses the channel into the basin, as demonstrated by the relative sediment volumes deposited along the confined channel at different slopes (see *Deposition in sloping confined channel* section, Fig. 10).

On entering the unconfined basin, the velocity profiles of the HDTCs at UVP 3 (Fig. 5A) indicate that currents initially continue to accelerate downstream of the SB-LOC, before decelerating further into the basin (as identified at UVP 4, Fig. 5A). In particular, the increase in velocity between UVP 2 and UVP 3 is attributed to a 'velocity lag' effect (Mulder & Alexander, 2001; Spychala *et al.*, 2020; Bell *et al.*, 2021), as the residual momentum of the turbidity currents gradually dissipates upon experiencing the reduction in slope angle occurring at the SB-LOC. This velocity lag coincides with a significant reduction in the elevation $H_{\max}$ of the maximum velocity $U = U_{\max}$ and the overall HDTC layer height $h_{\max}$ relative to the bed (Fig. 5A, UVP 2 → UVP 3). Flow relaxation downstream

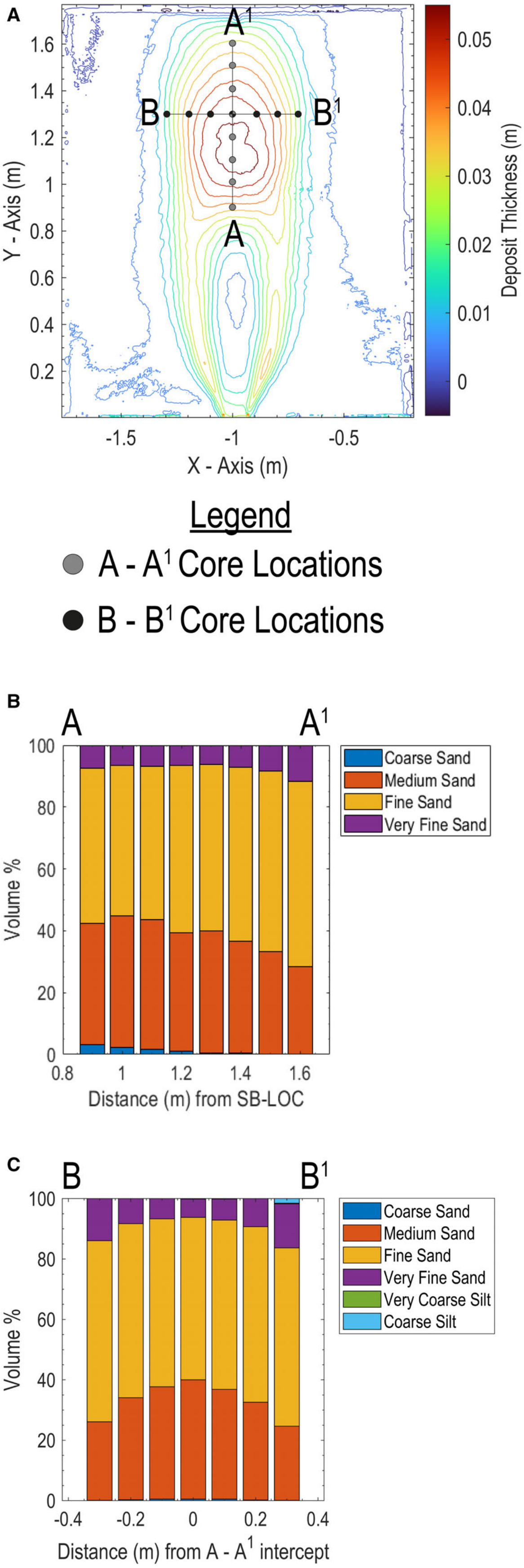

Fig. 13. (A) Contour plot of a typical basin deposition showing the location of bed cores taken for grain-size distribution analysis along transects (B) A–A^1 (i.e. centreline axis of deposit) and (C) B–B^1 (i.e. lateral axis at maximum deposit width) for run R1.3 (i.e. channel slope = 9°, $c_0 = 16\%$, Table 1).

of the SB-LOC is the driver of these height reductions as the HDTCs are no longer confined by the channel walls, which prevent the formation of lateral density gradients (Pohl *et al.*, 2019). After the SB-LOC, these density gradients drive lateral expansion of the HDTCs in the downstream unconfined basin, resulting in reductions of both $H_{\max}$ and $h_{\max}$. When combined with the velocity lag effect, this flow relaxation also explains the significant increase in the shear velocity U_* of the HDTCs at UVP 3 (Fig. 8), that corresponds with a switch from a depositional to a bypassing state in all runs, and hence the formation of a sediment bypass zone immediately downstream of the SB-LOC (Fig. 3D). Flow relaxation may also contribute to the velocity lag as the rapid reduction in $h_{\max}$ (i.e. UVP 2 → UVP 3, Fig. 5A) also corresponds with the conversion of potential energy E_p to kinetic energy E_k downstream of the LOC (Fig. 9). This energy conversion within other gravity-driven flows (for example, saline density currents) undergoing a LOC has previously been termed the 'slumping phase' (Huppert & Simpson, 1980), from the initial stage of density current expansion in lock-exchange experiments (Inghilesi *et al.*, 2018; Lombardi *et al.*, 2018).

In the current study, the combination of flow relaxation and velocity lag results in supercritical densimetric Froude numbers Fr_D for the HDTCs that increase significantly in response to the SB-LOC at the channel–basin transition, and remain strongly supercritical at UVP 4 (i.e. 0.6 m downstream of the SB-LOC) (Fig. 7C and D). This is true for all HDTCs in this study, irrespective of the slope break severity (i.e. channel slope angle) or the initial volumetric sediment concentration c_0 that generates the HDTCs. This poses the question as to where the downstream transition from supercritical ($\mathrm{Fr}_D > 1$) to subcritical ($\mathrm{Fr}_D < 1$) flow regimes may occur within the horizontal basin. This is important as previous experimental studies (e.g. Garcia & Parker, 1989; Baas *et al.*, 2004; Islam & Imran, 2010) have shown that sudden reductions in slope angle can induce internal hydraulic jumps, where turbidity currents transition rapidly from a supercritical ($\mathrm{Fr}_D > 1$) to subcritical ($\mathrm{Fr}_D < 1$) regime. In such cases, hydraulic jumps have been observed to form immediately downstream of a slope break, with the turbidity currents often depletive in nature (i.e. non-erosive and continually depositing) and decelerating on approach to the slope break. The resulting internal hydraulic jumps cause the currents to rapidly lose kinetic energy due to energy dissipation, as they decelerate rapidly and thicken (Komar, 1971; Baas *et al.*, 2004). As these studies have been for laterally constrained (i.e. 2D) channels, they have not considered the effects of lateral spreading of the current (Kostic & Parker, 2006) or the flow obstruction caused by sediment deposition. The latter effect may also induce a hydraulic jump through the interaction of the current with an adversely orientated topographic feature, resulting in rapid flow deceleration. As such, hydraulic jumps are not always synonymous with breaks in slope, particularly in 3D experiments and simulations. For example, Kostic & Parker (2006) found that the rapid deposition of sediment can prevent turbidity currents from going through a rapid supercritical to subcritical flow regime transition via a strong hydraulic jump. Alexander *et al.* (2008) also showed that dilute TCs (i.e. volumetric concentration of 1.21% and velocity of *ca* 0.10 m s^{-1}) can temporarily accelerate downstream of a SB-LOC if sufficient momentum has been generated on a high angle slope (20°).

The potential presence of larger hydraulic jumps immediately downstream of channel mouths, such as those observed by Garcia & Parker (1989), Garcia (1993), Baas *et al.* (2004) and Islam & Imran (2010) is not being questioned here. However, it is proposed that not all turbidity currents will necessarily produce internal hydraulic jumps immediately downstream of a SB-LOC. In the current study, the most likely location of the internal hydraulic jump appears to be further into the horizontal basin, downstream of UVP 4, close to the location of maximum deposition depth within the basin lobe element. Unfortunately, this can only be inferred as no such features have been observed or measured directly within the UVP data. However, the velocity profiles at UVP 4 generally show the HDTCs to be decelerating and, together with a corresponding increase in the height $H_{\max}$ of the maximum velocity $U_{\max}$, indicate a reduction in the bed shear velocity U_*. Consequently, supercritical HDTCs will only undergo flow regime transitions (i.e. via an internal hydraulic jump) when sufficient change occurs in the HDTC hydrodynamics, for example, when the current encounters an adverse slope or when it is ponded by severe downstream topography, resulting in rapid flow deceleration (e.g. Pohl *et al.*, 2020a; Soutter *et al.*, 2021). This indicates that the distance downstream of a SB-LOC at which the hydraulic jump occurs will not only depend on an adjustment length scale to the new slope angle (SB) and/or any change to lateral confinement (LOC), but it is also affected by other topographic bed features (for example, lobes) that the current interacts with during this adjustment.

Deposits of channelized turbidity currents

The thin sediment layers deposited in the confined channel at the highest bed slope angle (i.e. 9°, Fig. 10A) indicate that, when sufficiently steep, the channel itself acts as a sediment bypass zone. Under this condition, the majority of the deposition along the channel from the HDTCs is observed to occur after the cessation of the water–sediment flow at the inlet manifold (i.e. during the diminishing turbidity current tail). The bed profile measurement along the confined channel also indicates that an inverse relationship exists between the channel deposit thickness and the initial suspended sediment concentration c_0. This is expected as the HDTCs generated under the largest c_0 values at the channel inlet have sufficient residual momentum to transport the vast majority of the sediment load into the basin under this high channel slope condition. By contrast, a reduction in the channel slope break angle from 9° → 6° (Fig. 10B) → 3° (Fig. 10C) results in an increasing proportion of the sediment load being deposited along the confined channel, with this deposition occurring continually throughout the full duration of each HDTC. One surprising aspect of these channel deposition profiles that is particularly evident at these lower slope breaks (i.e. 6° and 3°, Fig. 10B and C) is that they appear to be largely unaffected by initial sediment concentration c_0. This suggests implicitly that a larger overall proportion of the sediment load contained in HDTCs formed from lower c_0 values (i.e. $c_0 = 12\%$) is deposited in the channel compared with HDTCs formed on the same channel slope condition from higher c_0 values (i.e. $c_0 = 18\%$). The along-channel deposition profiles indicate the formation of an adverse slope 0.5 to 1.0 m downstream of the inlet, with the largest deposit thicknesses, in all cases, occurring *ca* 1.30 m downstream of the inlet. This finding suggests that, on expansion away from the channel inlet, the HDTCs quickly become over capacity [with capacity defined as the maximum sediment concentration that the HDTC can transport in suspension (Kuenen & Sengupta, 1970)]. This is evident in the along-channel sediment deposition profiles at the lower slope conditions where, after an initial adjustment length on leaving the inlet, there is a rapid increase in deposition thickness (between *ca* 0.6 m → *ca* 1.30 m from the inlet), followed by a more gradual reduction in deposit thickness towards the SB-LOC. This downstream tapering of the deposit profile towards the SB-LOC indicates that the HDTCs are no longer over capacity, with deposition instead dominated by competency driven processes [i.e. where competency refers to the maximum supportable grain size that the HDTC can transport in suspension (Kuenen & Sengupta, 1970)]. The gradual loss of competency therefore leads to deposition of the coarser grain sizes from the initial suspended sediment size distribution, supported by high Rouse numbers calculated in the confined channel for the D_{90} percentile (Fig. 8) and evidenced by the lack of coarse sediment in core samples taken from the basin deposits (see *Deposit grain-size trends* section and Fig. 13).

Depositional features downstream of the SB-LOC

To aid the comparison of the deposits downstream of the SB-LOC to those of natural systems, the lobe hierarchy of Prélat *et al.* (2009) is considered. This scheme breaks down a lobe complex into four fundamental components (Fig. 14): (i) *beds*, which are the depositional product of individual TC events; (ii) *lobe elements*, formed by the stacking of multiple beds and generally no more than a few kilometres in length and width, and a few metres in thickness (Prélat *et al.*, 2009); (iii) *lobes*, produced by the stacking of one or more lobe elements fed from a single channel; and (iv) *lobe complexes*, produced as lobes switch via an upstream avulsion or channel migration, and stack or onlap onto older lobes (Ferguson *et al.*, 2020). By definition, individual HDTCs within this study produce *beds* as the deposits are formed by singular events. However, these basin deposits and those of similar experiments have a strong resemblance to *lobe elements* (Prélat *et al.*, 2009; Ferguson *et al.*, 2020; Spychala *et al.*, 2020). Such lobate deposits are therefore considered to be lobe elements (Fig. 14), while the corresponding sediment bypass zones are considered to be equivalent to lobe element scale channel–lobe transition zones (CLTZs).

Effect of experimental parameters on the geometry of lobe elements

At a given slope break condition (i.e. 9°, Fig. 10A to D), the resulting basin lobe element geometries become longer, wider and thicker (i.e. increasing L_L, W_L and D_L, Table 2) as the initial sediment concentration c_0 increases from 12 to 18%. Increases in these lobe dimensions are driven primarily by the increased volume of suspended sediment within the HDTCs for higher c_0 values that bypasses the confined channel and is deposited in the basin. For example, at the slope break angle of 9°, HDTCs generated with $c_0 = 12\%$ and 18% transported 80% and 95.82%, respectively, of the total sediment volume introduced into the channel–basin system (i.e. 0.0217 m^3 for $c_0 = 12\%$ and 0.032 m^3 for $c_0 = 18\%$) into the basin. In this context, HDTCs generated under higher c_0 values clearly have a much larger volume of sediment that bypasses the confined channel and is thus available to develop the lobe elements downstream of the SB-LOC. The effect of reducing the slope break angle from 9° → 6° → 3° is that the resulting basin lobe element geometries in general become shorter, narrower and thinner (i.e. reducing L_L, W_L and D_L, Table 2). This overall decrease in the size of basin lobe elements is attributed primarily to the increased volume of deposition that takes place within the confined channel as HDTCs become less able to bypass the initial volumetric sediment concentration c_0 beyond the SB-LOC. This is clearly demonstrated by the significant increase in channel deposition by HDTCs at lower bed slopes (for the same initial sediment concentration c_0). For example, for runs with $c_0 = 18\%$, in-channel deposition from the HDTCs generated increases from 4.2% (at 9° slope) → 31.2% (at 6° slope) → 43.0% (at 3° slope), indicating that the bypassed sediment volume beyond the SB-LOC reduces from 95.8% → 68.8% → 57.0%, respectively.

The relatively low proportions of coarse sand within the grain-size analysis also alludes to the HDTCs depositing the coarsest sediment fractions on the confined channel slope. This is supported by the estimated Rouse numbers for the D_{90} percentile of the initial suspended sediment mixture, which lie within the 50%

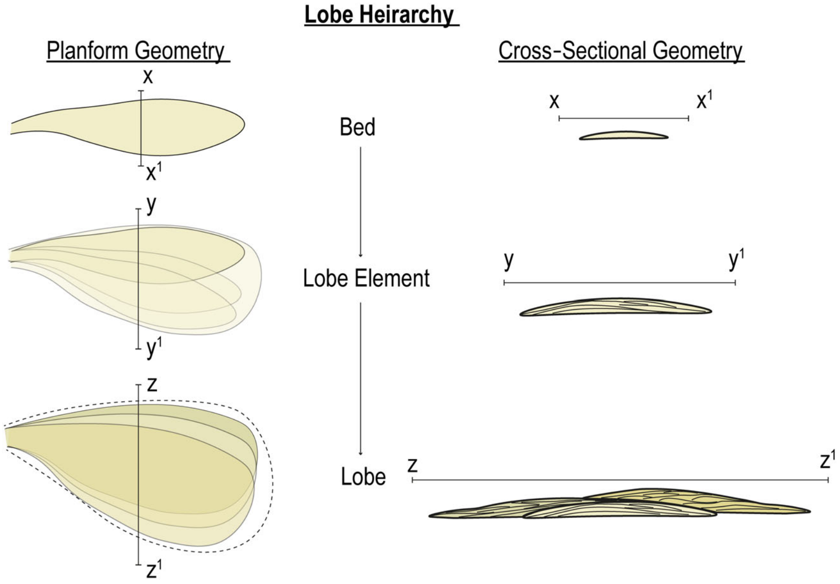

Fig. 14. Schematic representation of lobe hierarchy (Prélat *et al.*, 2009). This figure is based on schematic diagrams from Spychala *et al.* (2020) and Pettinga *et al.* (2018).

suspended sediment regime at UVP 1 and UVP 2 locations (Fig. 8). It is interesting to note that the overall grading of all sediment samples obtained from the lobe deposits are considerably coarser than the grain-size distribution of the initial sediment mixture (i.e. D_{10} : D_{50} : D_{90} = 90 : 163 : 284 μm). This indicates that a proportion of the finer sediment grain sizes completely bypass the whole channel–basin system and are deposited within the trough at the end of the basin section.

Comparison of lobe geometries produced in the current study with those developed in previous analogous experimental studies are shown in Table 3. These previous studies have generally indicated that an increase in the initial concentration c_0 (for a given channel–basin slope combination) tends to result in lobe elements that have a higher aspect ratio L_L/W_L, on account that denser HDTCs have greater runout distances. This runout distance (and hence L_L/W_L value) is also increased by increasing: (i) the channel slope angle (e.g. Baas *et al.*, 2004; Table 3); and (ii) the basin floor angle on which the lobe deposits are formed (e.g. Spychala *et al.*, 2020; Table 3). These previous findings are somewhat contradictory to the current study, where: (i) an inverse relationship exists between c_0 and the lobe deposit aspect ratio L_L/W_L (i.e. L_L/W_L generally reduces with increasing c_0, at a fixed channel slope condition); and (ii) a reduction in the channel slope increases L_L/W_L (for a given c_0 value). Overall, the range of aspect ratios L_L/W_L = 2.39–3.16 obtained in the current study are found to be significantly higher than in Baas *et al.* (2004), where L_L/W_L = 1.10–2.09 for depletive turbidity currents that formed internal hydraulic jumps immediately downstream of the SB-LOC. These depletive currents are thus dynamically different to the supercritical HDTCs in the current study that have much longer run-out distances into the basin (and, hence, higher L_L/W_L values). By contrast, the lobe aspect ratios measured by Spychala *et al.* (2020) (i.e. L_L/W_L = 1.66–3.66, Table 3) are in more general agreement with the current study. Their study also indicates that a similar relationship exists between sediment bypass into the basin, the slope angle and the sediment concentration in the turbidity current (as discussed above), with higher discharge conditions also resulting in lobe deposits that are fully detached from the simulated channel–levée system. The experimental results in the current study also broadly agree with a range of natural scale lobe elements identified by Pettinga *et al.* (2018) and Saller *et al.* (2008) to have aspect ratios L_L/W_L between 0.61–10.73 (average = 2.59, n = 38) and 1.0–7.2 (average = 2.18, n = 18), respectively.

Table 3. Geometrical dimensions of lobe elements measured in previous experimental studies, detailing key experimental parameters and resulting length to width ratios. (Note: Lock Ex. refers to a lock exchange experiment, and NR refers to values not reported.)

Study	Initial conc. (%)	Slope angle (°)	Basin floor angle (°)	Flow rate ($m^3 h^{-1}$)	Flow volume (m^3)	L_L (m)	W_L (m)	D_L (m)	L_L/W_L
Spychala *et al.* (2020)	17	11	0	30	0.90	3.10	1.86	0.088	1.66
	17	11	1	30	0.90	3.35	1.81	0.075	1.84
	17	11	2	30	0.90	3.57	1.52	0.066	2.34
	17	11	3	30	0.90	3.83	1.56	0.066	2.45
	17	11	4	30	0.90	4.44	1.43	0.062	3.10
	19	11	4	30	0.90	4.65	1.38	0.078	3.36
	15	11	4	30	0.90	3.90	1.43	0.056	2.72
	13	11	4	30	0.90	3.40	1.23	0.056	2.76
	17	11	4	25	0.90	3.70	1.17	0.056	3.16
	17	11	4	40	0.90	4.30	1.26	0.069	3.14
Bell *et al.* (2021)	17	11	4	40	0.90	4.60	2.00	0.065	2.30
Luthi, (1981)	4	5	5	12.6	0.25	4.59	2.50	0.01	1.83
Al Ja'aidi *et al.* (2004)	8	0	0	Lock Ex.	0.0046	NR	NR	NR	0.75
	11	0	0	Lock Ex.	0.0046	NR	NR	NR	1.00
	13	0	0	Lock Ex.	0.0046	NR	NR	NR	1.40
	15	0	0	Lock Ex.	0.0046	NR	NR	NR	1.19
	16	0	0	Lock Ex.	0.0046	NR	NR	NR	1.13
	8	0	0	Lock Ex.	0.0046	NR	NR	NR	0.71
	8	0	0	Lock Ex.	0.0050	NR	NR	NR	1.00
	8	0	0	Lock Ex.	0.0051	NR	NR	NR	1.09
	8	0	0	Lock Ex.	0.0060	NR	NR	NR	1.27
Baas *et al.* (2004)	27.0	8.6	0	28.0	0.158	NR	NR	NR	1.87
	35.0	8.6	0	28.0	0.179	NR	NR	NR	2.09
	14.0	8.6	0	28.0	0.136	NR	NR	NR	1.71
	21.1	3.7	0	18.7	0.100	NR	NR	NR	1.11
	31.7	3.7	0	28.0	0.110	NR	NR	NR	1.20
	31.7	3.7	0	28.0	0.110	NR	NR	NR	1.17
	42.2	3.7	0	28.0	0.121	NR	NR	NR	1.10
	21.2	3.7	0	18.7	0.100	NR	NR	NR	1.21
Fernandez *et al.*, (2014)	5	4	1.5	0.06	0.076	1.37	0.61	0.025	2.24
	5	4	1.5	0.06	0.095	1.23	0.85	0.022	1.44
	5	4	1.5	0.06	0.076	0.60	0.50	0.020	1.20
	5	4	1.5	0.06	0.057	0.30	0.24	0.005	1.25
	5	4	1.5	0.06	0.095	0.88	0.49	0.013	1.79
Wilkin *et al.* (this study)	12	9	0	13.0	0.18	1.58	0.54	0.042	2.92
	14	9	0	12.7	0.18	1.66	0.57	0.049	2.91
	16	9	0	12.8	0.18	1.69	0.63	0.057	2.68
	18	9	0	12.8	0.18	1.70	0.71	0.060	2.39
	12	6	0	12.7	0.18	1.45	0.48	0.036	3.02
	14	6	0	12.7	0.18	1.55	0.49	0.045	3.16
	16	6	0	12.6	0.18	1.58	0.54	0.054	2.92
	18	6	0	12.7	0.18	1.65	0.61	0.064	2.70
	12	3	0	13.8	0.19	1.42	0.45	0.035	3.15
	18	3	0	13.6	0.19	1.69	0.58	0.060	2.91

Effect of experimental parameters on the geometry of CLTZs

In all experimental runs, the sediment deposits within the sloping confined channel are fully detached from the lobe deposits in the horizontal basin by a sediment bypass region immediately downstream of the SB-LOC (Fig. 11), as representative of the channel–lobe transition zone (CLTZ).

Table 4. Comparative channel mouth bypass zone dimensions and aspect ratios obtained from both modern (*M*) and ancient (*A*) field scale erosional and depositional features and the equivalent dimension and aspect ratio ranges from the current laboratory (*L*) studies.

Location	Study	Length (L_B)	Width (W_B)	Depth (D_B)	L_B/W_B
Karoo Basin (A)	Hansen *et al.* (2021)	2 km	4 km	28 m	0.5
Makran Margin (M)	Bourget *et al.* (2011)	20 km 15 km	8 km 7 km	300 m 150 m	2.5 2.14
Bahamas Banks (M)	Schnyder *et al.* (2018), Recouvreur *et al.* (2021)	100 to 650 m	80 to 360 m	>20 m	~1.34
Niger Delta Slope (A)	Prather *et al.* (2012)	>1 km	~500 m		~2
California Margin, Los Angeles Margin, & New Jersey Margin (M)	Lee *et al.* (2002)	<1.1 km	~400 m	~21 m	2.5–0.4
Peïra Cava outlier (A)	Lee *et al.* (2004)	>1 km	~400 m	>20 m	~2.5
Cascadia Wedge (M)	Beeson *et al.* (2017)	5.47 km	6.4 km	~43 m	0.85
This study (L)		0.66 to 0.86 m	0.24 to 0.36 m	0.015 to 0.03 m	2.06 to 3.37

Analysis of the geometry of these CLTZs (Fig. 12) shows that an increase in the initial sediment concentration c_0 typically reduces the non-dimensional aspect ratios L_B/W_B and L_B/D_B of the CLTZs (Table 2). For example, for runs conducted at the 9° channel slope condition, L_B/W_B and L_B/D_B decrease from 2.80 → 2.36 and 42.0 → 28.66, respectively, as $c_0 = 12\% \rightarrow 18\%$. By contrast, the effect of reducing the channel slope angle from $9° \rightarrow 6° \rightarrow 3°$ corresponds to a gradual reduction in the CLTZ length L_B produced by HDTCs with comparable initial sediment concentrations c_0, while changes to W_B and D_B are less consistent (Table 2).

It is also informative to consider how the aspect ratios L_B/W_B of the bypass zones produced in the current study (Table 2) compare with others from similar channel mouth settings (Hodgson *et al.*, 2022). Based upon the results obtained, it is perceived that the channel mouth setting modelled in the current study has hydrodynamic characteristics analogous to both supercritical channel–lobe transition zones and plunge pools. Hodgson *et al.* (2022) note that both of these features are generated by supercritical flows and the bypass zone produced by the HDTCs of this study shares similar geometrical properties with the latter (Table 4). In general, the L_B/W_B values in the current study (i.e. 2.06–3.37, Table 2) coincide with the upper end of the equivalent L_B/W_B value range (i.e. 0.4–2.5, Table 4) observed for natural CLTZ systems, thus indicating some degree of accord across scales.

Overall, the CLTZ and basin lobe geometries are indicative of the complex relationship that exists between the HDTC dynamics (for example, flow velocities, shear velocities, Froude numbers and energy transitions) under different experimental conditions (for example, slope break angle and initial concentration c_0) and the relative proportions of the sediment load that: (i) deposit along the confined channel; and (ii) bypass the SB-LOC to be deposited in the basin lobe. Indeed, it can be concluded that the scaling complexities that exist between the HDTC flow dynamics and the resulting non-dimensional aspect ratios for both the CLTZs (i.e. L_B/W_B; L_B/D_B) and the basin lobes (i.e. L_L/W_L; L_L/D_L) most likely arise from the counteracting effects of the channel slope break and loss of confinement. Specifically, the slope break (SB) clearly results in deceleration of the HDTC, flow thickening and a reduction in the shear velocity, while the loss of confinement (LOC) results in acceleration of the HDTC, a reduction in the flow thickness, and an increase in shear velocity. A combination of these effects at the SB-LOC may well at least partly account for the lack of clear scaling patterns within the resulting CLTZs and lobe deposits.

CONCLUSIONS

Scaled laboratory experiments are conducted to investigate how supercritical high density turbidity currents (HDTCs) and their deposits are influenced by an abrupt transition between a confined, sloping channel and an unconfined, horizontal, basin. The key focus of the study is to determine the response of turbidity current flow dynamics and deposition geometries within the channel–basin system to changes in the initial volumetric suspended sediment concentration and the slope break angle at a simultaneous loss of confinement (i.e. SB-LOC). This is relevant to understanding the hydrodynamic and depositional variability within deep water sedimentary systems, particularly those associated with channel mouth settings such as supercritical channel–lobe transition zones and plunge pools.

Velocity and concentration profile measurements within the HDTCs demonstrate that an increase in the initial volumetric sediment concentration (for a particular slope break condition) results in higher along-channel flow velocities both in the laterally confined (2D) sloping channel and the unconfined (3D) horizontal basin. A reduction in the slope break angle at the simultaneous SB-LOC (for the same initial sediment concentration condition), by contrast, results in an overall decrease in the current velocity. Concentration measurements within the HDTCs immediately downstream of the SB-LOC also show a systematic increase with increasing initial sediment concentration, but only a marginal reduction as the slope break angle is reduced.

The hydrodynamics of the HDTCs in the channel–basin system are also characterized by downstream variations in the shear velocity, densimetric Froude number, and the potential and kinetic energy. Importantly, the HDTCs are shown to remain supercritical throughout the system, and exhibit an increase to their densimetric Froude number and shear velocity due to both flow relaxation and residual momentum immediately downstream of the SB-LOC. These flow relaxation and momentum effects are believed to be analogous to the slumping phase observed as 3D gravity-driven flows expand laterally following lock release into an unconfined basin, and coincide with the conversion of potential energy to kinetic energy. In the current study, the HDTCs experience a short period of velocity lag on encountering the SB-LOC, during which they continue to accelerate into the basin. The overall thickness of the HDTCs, along with the height within the current at which maximum velocities occur, also reduce significantly immediately downstream of the SB-LOC. The resulting increase in the bed shear velocity produces a zone of sediment bypass that is analogous to a channel–lobe transition zone (CLTZ) that detaches the channel and basin deposits. This study therefore has important implications for the hydrodynamic processes that govern the formation and preservation of stratigraphy within CLTZs, and affirms the need of further research to help link the hydrodynamic behaviour of HDTCs and the resulting channel and basin deposit geometries within these settings. The dimensions of the CLTZs produced by HDTCs are shown to be impacted by the channel slope break angle and the initial sediment concentration, with a reduction in the slope break resulting in CLTZs with reduced dimensions (i.e. length, width and depth). By contrast, an increase in the initial sediment concentration results in CLTZs that have a more circular geometry, as demonstrated by a reduction in the measured aspect ratio L_B/W_B for the sediment bypass regions.

Basin lobe elements that are fully detached from the channel slope deposits by the CLTZs, typically increase in size (i.e. length, width and thickness), with their centroid located further downstream of the SB-LOC, as the initial sediment concentration is increased (for a given slope break condition). Conversely, a reduction in the slope break angle (for a given initial sediment concentration) results in basin lobe elements that are typically shorter, narrower and thinner. This occurs as the sediment bypass efficiency of HDTCs is reduced at lower slope angles, meaning that an increased proportion of the sediment load is deposited within the confined channel, upstream of the SB-LOC. Grain-size analysis of cores obtained along the axial centreline of the basin lobe elements and across the lobe deposits at their maximum thicknesses, shows that general fining occurs both in the downstream direction and laterally (in both directions) away from the centreline deposit axis. The measured grain-size distributions also indicate that the coarsest sediment fraction (i.e. coarse sand) is largely absent from the lobe deposits, suggesting that it must be deposited in the confined channel, prior to the SB-LOC, as predicted by the Rouse numbers for the D_{90} percentile of the sediment mixture.

In summary, the scaled experimental study provides a plausible explanation for the sediment bypass zones and basin lobe deposits produced by supercritical high density turbidity currents as they undergo a simultaneous loss of confinement and break of slope, highlighting the geometrical dependencies. Results indicate that these sedimentary features need not always be formed by internal hydraulic jumps, but may instead result from flow relaxation of the turbidity currents during the transition from confined sloping channels to unconfined basin floors. This transition is characterized by the continued acceleration of turbidity currents during a period of velocity lag, during which flow relaxation takes place, causing a reduction in current thickness and elevated shear velocities. Results therefore have important implications for the stratigraphy associated with rapid channel mouth transitions, such as supercritical channel–lobe transition zones and plunge pools, as this study indicates that these zones may be characterized by increased densimetric Froude numbers. Future work should focus on the longevity of these bypass features, and the relationship between the feeder channel and CLTZ geometry.

ACKNOWLEDGEMENTS

This work has been conducted by JW as part of his PhD project on the Natural Environment Research Council (NERC) Centre for Doctoral Training (CDT) programme in Oil & Gas [NEM00578X/1]. The authors would like to thank the reviewers of the original manuscript (J. Eggenhuisen, F. Pohl and C. Stevenson). Their insightful and detailed commentaries and suggested improvements have greatly enhanced the resulting paper. There are no known conflicts of interest.

DATA AVAILABILITY STATEMENT

The data that support the findings of this study are available from the corresponding author upon reasonable request.

REFERENCES

Al Ja'Aidi, O.S., **McCaffrey, W.D.** and **Kneller, B.C.** (2004) Factors influencing the deposit geometry of experimental turbidity currents: implications for sand-body architecture in confined basins. *Geol. Soc. Spec. Pub.*, **222**, 45–58.

Alexander, J., **McLelland, S.J.**, **Gray, T.E.**, **Vincent, C.E.**, **Leeder, M.R.** and **Ellett, S.** (2008) Laboratory sustained turbidity currents form elongate ridges at channel mouths. *Sedimentology*, **55**, 845–868.

Amy, L.A., **Kneller, B.C.** and **McCaffrey, W.D.** (2007) Facies architecture of the Grès de Peïra cava, SE France: landward stacking patterns in ponded turbiditic basins. *J. Geol. Soc. London*, **164**, 143–162.

Azpiroz-Zabala, M., **Cartigny, M.J.B.**, **Talling, P.J.**, **Parsons, D.R.**, **Sumner, E.J.**, **Clare, M.A.**, **Simmons, S.M.**, **Cooper, C.** and **Pope, E.L.** (2017) Newly recognized turbidity current structure can explain prolonged flushing of submarine canyons. *Sci. Adv.*, **3**, 1–12.

Baas, J.H., **Wessel, V.K.** and **Postma, G.** (2004) Deposits of depletive high-density turbidity currents: a flume anolouge of bed geometry, structure and texture. *Sedimentology*, **51**, 1053–1088.

Beeson, J.W., **Goldfinger, C.** and **Fortin, W.F.** (2017) Large-scale modificaiton of submarine geomorphic features on the Cascadia accretionary wedge caused by catastrophic flooding events. *Geosphere*, **13**, 1713–1728.

Bell, D., **Soutter, E.L.**, **Cumberpatch, Z.A.**, **Ferguson, R.A.**, **Spychala, Y.T.**, **Kane, I.A.** and **Eggenhuisen, J.T.** (2021) Flow-process controls on grain type distribution in an experimental turbidity current deposit: implications for detrital signal preservation and microplastic distribution in submarine fans. *Deposit. Rec.*, **7**, 392–415.

Blott, S.J. and **Pye, K.** (2001) Gradistat: A grain size distribution and statistics package for the analysis of unconsolidated sediments. *Earth Surf. Process. Landf.*, **26**, 1237–1248.

Bourget, J., **Zaragosi, S.**, **Ellouz-Zimmermann, N.**, **Mouchot, N.**, **Garlan, T.**, **Schneider, J.L.**, **Lanfumey, V.** and **Lallemant, S.** (2011) Turbidite system architecture and sedimentary processes along topographically complex slopes: the Makran convergent margin. *Sedimentology*, **58**, 376–406.

Boyer, F., **Guazzelli, É.** and **Pouliquen, O.** (2011) Unifying suspension and granular rheology. *Phys. Rev. Lett.*, **107**, 1–5.

Brooks, H.L., **Hodgson, D.M.**, **Brunt, R.L.**, **Peakall, J.**, **Poyatos-Moré, M.** and **Flint, S.S.** (2018a) Disconnected submarine lobes as a record of stepped slope evolution over multiple sea-level cycles. *Geosphere*, **14**, 1753–1779.

Brooks, H.L., **Hodgson, D.M.**, **Brunt, R.L.**, **Peakall, J.**, **Hofstra, M.** and **Flint, S.S.** (2018b) Deep-water channel-lobe transition zone dynamics: processes and depositional architecture, an example from the Karoo Basin, South Africa. *GSA Bull.*, **130**, 1723–1746.

Brooks, H.L., **Ito, M.**, **Zuchuat, V.**, **Peakall, J.** and **Hodgson, D.M.** (2022) Channel-lobe transition zone development in tectonically active settings: implications for hybrid bed development. *Deposit. Rec.*, **8**, 829–868.

Cartigny, M.J.B., **Eggenhuisen, J.T.**, **Hansen, E.W.M.** and **Postma, G.** (2013) Concentration-dependent flow stratification in experimental high-density turbidity currents and their relevance to turbidite facies models. *J. Sediment. Res.*, **83**, 1046–1064.

Carvajal, C., **Paull, C.K.**, **Caress, D.W.**, **Fildani, A.**, **Lundsten, E.**, **Anderson, K.**, **Maier, K.L.**, **McGann, M.**, **Gwiazda, R.** and **Herguera, J.C.** (2017) Unraveling the channel–lobe transition zone with high-resolution AUV bathymetry: Navy Fan, Offshore Baja California, Mexico. *J. Sediment. Res.*, **87**, 1049–1059.

Cheng, N. (1997) Simplified settling velocity formula for sediment particle. *J. Hydraul. Eng.*, **123**, 149–152.

Clarke, J.E.H. (2016) First wide-angle view of channelized turbidity currents links migrating cyclic steps to flow characteristics. *Nat. Commun.*, **7**, 11896.

Cumberpatch, Z.A., **Kane, I.A.**, **Soutter, E.L.**, **Hodgson, D.M.**, **Jackson, C.A.L.**, **Kilhams, B.A.** and **Poprawski, Y.** (2021) Interactions between deep-water gravity flows and active salt tectonics. *J. Sediment. Res.*, **91**, 34–65.

De Leeuw, J., **Eggenhuisen, J.T.** and **Cartigny, M.J.B.** (2016) Morphodynamics of submarine channel inception revealed by new experimental approach. *Nat. Commun.*, **7**, 1–7.

De Leeuw, J., **Eggenhuisen, J.T.**, **Spychala, Y.T.**, **Heijnen, M.S.**, **Pohl, F.** and **Cartigny, M.J.B.** (2018) Sediment volume and grain-size partitioning between submarine channel-levee systems and lobes: an experimental study. *J. Sediment. Res.*, **88**, 777–794.

Dorrell, R.M., **Peakall, J.**, **Sumner, E.J.**, **Parsons, D.R.**, **Darby, S.E.**, **Wynn, R.B.**, **Özsoy, E.** and **Tezcan, D.** (2016) Flow dynamics and mixing processes in hydraulic jump arrays: implications for channel-lobe transition zones. *Mar. Geol.*, **381**, 181–193.

Ferguson, R.A., **Kane, I.A.**, **Eggenhuisen, J.T.**, **Pohl, F.**, **Tilston, M.**, **Spychala, Y.T.** and **Brunt, R.L.** (2020) Entangled external and internal controls on submarine fan evolution: an experimental perspective. *Deposit. Rec.*, **6**, 605–624.

Fernandez, R.L., **Cantelli, A.**, **Primez, C.**, **Sequeiros, O.** and **Parker, G.** (2014) Growth patterns of subaqueous depostional channel lobe systems developed over a basement with a downdip break in slope: laboratory experiments. *J. Sediment. Res.*, **84**, 168–182.

Fildani, A., **Hubbard, S.M.**, **Covault, J.A.**, **Maier, K.L.**, **Romans, B.W.**, **Traer, M.** and **Rowland, J.C.** (2013) Erosion at inception of deep-sea channels. *Marine Petrol. Geol.*, **41**, 48–61.

Garcia, M. (1993) Hydraulic jumps in sediment-driven bottom currents. *J. Hydraul. Eng.*, **119**, 1094–1117.

Garcia, M. and **Parker, G.** (1989) Experiments on hydraulic jumps in turbidity currents near a canyon-fan transition. *Science*, **245**, 393–396.

Gardner, M.H., **Borer, J.M.**, **Melick, J.J.**, **Mavilla, N.**, **Dechesne, M.** and **Wagerle, R.N.** (2003) Stratigraphic process – response model for submarine channels and related features from studies of Permian brushy canyon outcrops, West Texas. *Mar. Petrol. Geol.*, **20**, 757–787.

Garnder, M.H., **Borer, J.M.**, **Romans, B.W.**, **Baptisa, N.**, **Kling, E.**, **Melick, J.**, **Wagerle, R.**, **Carr, M.**, **Schofield, K.** and **Rosen, N.** (2008) Stratigraphic models for Deepwater sedimentary systems. In: *Answering the Challenges of Production from Deep-Water Reservoirs: Analouges and Case Histories to Aid a New Generation* (Eds Schofield, K., Rosen, N., Pfeiffer, D. and Johnson, S.), *28th Annual Gulf Coast Section – SEPM Foundation Bob F. Perkins Research Conference, Houston, Texas*, **28**, 77–175.

Ge, Z., **Nemec, W.**, **Gawthorpe, R.L.** and **Hansen, E.W.M.** (2017) Response of unconfined turbidity current to normal-fault topography. *Sedimentology*, **64**, 932–959.

Gray, T.E., **Alexander, J.** and **Leeder, M.R.** (2006) Longitudinal flow evolution and turbulence structure of dynamically similar, sustained, saline density and turbidity currents. *J. Geophys. Res. Oceans*, **111**, 1–14.

Guiastrennec-Faugas, L., **Gillet, H.**, **Peakall, J.**, **Dennielou, B.**, **Gaillot, A.** and **Jacinto, R.S.** (2021) Initiation and evolution of knickpoints and their role in cut-and-fill processes in active submarine channels. *Geology*, **49**, 314–319.

Hage, S., **Galy, V.V.**, **Cartigny, M.J.B.**, **Acikalin, S.**, **Clare, M.A.**, **Gröcke, D.R.**, **Hilton, R.G.**, **Hunt, J.E.**, **Lintern, D.G.**, **Mcghee, C.A.**, **Parsons, D.R.**, **Stacey, C.D.**, **Sumner, E.J.** and **Talling, P.J.** (2020) Efficient preservation of young terrestrial organic carbon in sandy turbidity-current deposits. *Geology*, **48**, 882–887.

Hansen, L.A.S., **Healy, R.S.**, **Gomis-Cartesio, L.**, **Lee, D.R.**, **Hodgson, D.M.**, **Pontén, A.** and **Wild, R.J.** (2021) The origin and 3D architecture of a km-scale deep-water scour-fill: example from the Skoorsteenberg Fm, Karoo Basin, South Africa. *Front. Earth Sci.*, **9**, 1–18.

Heerema, C.J., **Talling, P.J.**, **Cartigny, M.J.**, **Paull, C.K.**, **Bailey, L.**, **Simmons, S.M.**, **Parsons, D.R.**, **Clare, M.A.**, **Gwiazda, R.**, **Lundsten, E.**, **Anderson, K.**, **Maier, K.L.**, **Xu, J.P.**, **Sumner, E.J.**, **Rosenberger, K.**, **Gales, J.**, **McGann, M.**, **Carter, L.** and **Pope, E.** (2020) What determines the downstream evolution of turbidity currents? *Earth Planet. Sci. Lett.*, **532**, 116023.

Hodgson, D.M., **Peakall, J.** and **Maier, K.L.** (2022) Submarine channel mouth settings: processes, geomorphology, and deposits. *Front. Earth Sci.*, **10**. https://doi.org/10.3389/feart.2022.790320.

Hofstra, M., **Hodgson, D.M.**, **Peakall, J.** and **Flint, S.S.** (2015) Giant scour-fills in ancient channel-lobe transition zones: formative processes and depositional architecture. *Sediment. Geol.*, **329**, 98–114.

Howlett, D.M., **Ge, Z.**, **Nemec, W.**, **Gawthorpe, R.L.**, **Rotevatn, A.** and **Jackson, C.A.L.** (2019) Response of unconfined turbidity current to deep-water fold and thrust belt topography: orthogonal incidence on solitary and segmented folds. *Sedimentology*, **66**, 2425–2454.

Howlett, D.M., **Gawthorpe, R.L.**, **Ge, Z.**, **Rotevatn, A.** and **Jackson, C.A.L.** (2020) Turbidites, topography and tectonics: evolution of submarine channel-lobe systems in the salt-influenced kwanza basin, offshore angola. *Basin Res.*, **33**, 1076–1110.

Huppert, H.E. and **Simpson, J.E.** (1980) The slumping of gravity currents. *J. Fluid Mech.*, **99**, 785–799.

Inghilesi, R., **Adduce, C.**, **Lombardi, V.**, **Roman, F.** and **Armenio, V.** (2018) Axisymmetric three-dimensional gravity currents generated by lock exchange. *J. Fluid Mech.*, **851**, 507–544.

Islam, M.A. and **Imran, J.** (2010) Vertical structure of contineous release saline and turbidity currents. *J. Geophys. Res.*, **115**, C08025.

Ito, M., **Ishikawa, K.** and **Nishida, N.** (2014) Distinctive erosional and depositonal structures formed at a channel mouth: A lower Pleistocene deep-water succession in the Kazusa forearc basin on the Boso peninsula, Japan. *Sedimentology*, **61**, 2042–2062.

Kane, I.A. and **Clare, M.A.** (2019) Dispersion, accumulation, and the ultimate fate of microplastics in deep-marine environments: A review and future directions. *Front. Earth Sci.*, **7**, 1–27.

Khripounoff, A., **Vangriesheim, A.**, **Babonneau, N.**, **Crassous, P.**, **Dennielou, B.** and **Savoye, B.** (2003) Direct observation of intense turbidity current activity in the Zaire submarine valley at 4000m water depth. *Mar. Geol.*, **194**, 151–158.

Komar, P.D. (1971) Hydraulic jumps in turbidity currents. *GSA Bull.*, **82**, 1477–1488.

Kostic, S. and **Parker, G.** (2006) The response of turbidity currents to a canyon–fan transition: internal hydraulic jumps and depositional signatures. *J. Hydraul. Res.*, **44**, 631–653.

Kuenen, P.H. and **Migliorini, C.I.** (1950) Turbidity currents as a cause of graded bedding. *J. Geol.*, **58**, 91–127.

Kuenen, P.H. and **Sengupta, S.** (1970) Experimental marine suspension currents. *Geologie Mijnb*, **49**, 89–118.

Launder, B.E. and **Rodi, W.** (1983) The Turbulent Wall jet measurements and modeling. *Annu. Rev. Fluid Mech.*, **15**, 429–459.

Lee, S.E., **Talling, P.J.**, **Ernst, G.G.J.** and **Hogg, A.J.** (2002) Occurrence and origin of submarine plunge pools at the base of the US continental slope. *Mar. Geol.*, **185**, 363–377.

Lee, S.E., **Amy, L.A.** and **Talling, P.J.** (2004) The character and origin of thick base-of-slope sandstone units of the Peïra cava outlier, SE France. *Geol. Soc. Spec. Pub.*, **221**, 331–347.

Lombardi, V., **Adduce, C.** and **La Rocca, M.** (2018) Unconfined lock-exchange gravity currents with variable lock width: laboratory experiments and shallow-water simulations. *J. Hydraul. Res.*, **56**, 399–411.

Luthi, S. (1981) Experiments on non-channelised turbidity currents and their deposits. *Mar. Geol.*, **40**, 59–68.

Macdonald, H.A., **Peakall, J.**, **Wignall, P.B.** and **Best, J.** (2011a) Sedimentation in deep-sea lobe-elements: implications for the origin of thickening-upward sequences. *J. Geol. Soc. London*, **168**, 319–331.

Macdonald, H.A., **Wynn, R.B.**, **Huvenne, V.A.I.**, **Peakall, J.**, **Masson, D.G.**, **Weaver, P.E.** and **McPhail, S.D.** (2011b) New insight into the morphology, fill, and remarkable longevity (>0.2 m.y.) of modern deep-water erosional scours along the Northeast Atlantic margin. *Geosphere*, **7**, 845–867.

Maier, K.L., **Paull, C.K.**, **Caress, D.W.**, **Anderson, K.**, **Nieminski, N.M.**, **Lundsten, E.**, **Erwin, B.E.**, **Gwiazda, R.** and **Fildani, A.** (2020) Submarine-fan development revealed by integrated high-resolution datasets from La Jolla Fan, offshore California, U.S.A. *J. Sediment. Res.*, **90**, 468–479.

Miramontes, E., **Eggenhuisen, J.T.**, **Jacinto, R.S.**, **Ponet, G.**, **Pohl, F.**, **Normandeau, A.**, **Campbell, C.D.** and **Hernández-Molina, F.J.** (2020) Channel – levee evolution in combined contour current – turbidity current flows from flume – tank experiments. *Geology*, **48**, 353–357.

Mulder, T. and **Alexander, J.** (2001) The physical character of subaqueous sedimentary density flow and their deposits. *Sedimentology*, **48**, 269–299.

Mutti, E. (1974) Examples of ancient deep-sea fan deposits from circum-Mediterranean geosynclines. In: *Modern and Ancient Geosynclinal Sedimentation* (Eds Dott, R.H., Jr. and Shaver, R.H.), *Soc. Econ. Paleont. Mineral. Spec. Publ*, **19**, 92–105.

Mutti, E. (1977) Distinctive thin-bedded turbidite facies and related depositional environments in the Eocene Hecho group (south-Central Pyrenees, Spain). *Sedimentology*, **24**, 107–131.

Mutti, E. (1985) Turbidite systems and their relations to depositional sequences. In: *Provenance of Arenites; NATO – ASI Series* (Ed. Zuffa, G.G.), pp. 65–93. Reidel, Dordrecht.

Mutti, E. and **Normark, W.R.** (1987) Comparing examples of modern and ancient turbidite systems: problems and concepts. In: *Marine Clastic Sedimentology: Concepts and Case Studies* (Eds Leggett, J.K. and Zuffa, G.G.), pp. 1–38. Graham and Troutman, London.

Navarro, L. and **Arnott, R.W.C.** (2020) Stratigraphic record in the transition from basin floor to continental slope sedimentation in the ancient passive-margin Windermere turbidite system. *Sedimentology*, **67**, 1710–1749.

Patel, U.S., **Gardiner, A.** and **Stow, D.A.V.** (2021) Bed-scale vertical and lateral distribution of massive sandstone in a topographically confined basin (Peïra cava, SE France): implications for flow processes. *Sediment. Geol.*, **424**, 106001.

Paull, C.K., **Talling, P.J.**, **Maier, K.L.**, **Parsons, D.**, **Xu, J.**, **Caress, D.W.**, **Gwiazda, R.**, **Lundsten, E.M.**, **Anderson, K.**, **Barry, J.P.**, **Chaffey, M.**, **O'Reilly, T.**, **Rosenberger, K.J.**, **Gales, J.A.**, **Kieft, B.**, **McGann, M.**, **Simmons, S.M.**, **McCann, M.**, **Sumner, E.J.** and **Cartigny, M.J.** (2018) Powerful turbidity currents driven by dense basal layers. *Nat. Commun.*, **9**, 1–9.

Pemberton, E.A.L., **Hubbard, S.M.**, **Filandi, A.**, **Romans, B.** and **Stright, L.** (2016) The stratigrphic expression of decreasing confinement along a deep-water sediment routing system: outcrop example from southern Chile. *Geosphere*, **12**, 114–134.

Penna, N., **D'Alessandro, F.**, **Gaudio, R.** and **Tomasicchio, G.R.** (2019) Three-dimensional analysis of local scouring induced by a rotating ship propeller. *Ocean Eng.*, **188**, 106294.

Pettinga, L., **Jobe, Z.**, **Shumaker, L.** and **Howes, N.** (2018) Morphometric scaling relationships in submarine channel-lobe systems. *Geology*, **46**, 819–822.

Pohl, F., **Eggenhuisen, J.T.**, **Tilston, M.** and **Cartigny, M.J.B.** (2019) New flow relaxation mechanism explains scour fields at the end of submarine channels. *Nat. Commun.*, **10**, 1–8.

Pohl, F., **Eggenhuisen, J.T.**, **Kane, I.A.** and **Clare, M.A.** (2020a) Transport and burial of microplastics in deep-marine sediments by turbidity currents. *Sci. Technol.*, **54**, 41808–44189.

Pohl, F., **Eggenhuisen, J.T.**, **Cartigny, M.J.B.**, **Tilston, M.C.**, **de Leeuw, J.** and **Hermidas, N.** (2020b) The influence of a slope break on turbidite deposits: an experimental investigation. *Mar. Geol.*, **424**, 106160.

Pohl, F., **Eggenhuisen, J.T.**, **Cartigny, M.** and **Tilston, M.** (2022) Initation of deposition in supercritical turbidity currents downstream of a slope break. *Eartharxiv*. https://doi.org/10.31223/X5M35X.

Postma, G., **Hoyal, D.C.**, **Abreu, V.**, **Cartigny, M.J.B.**, **Demko, T.**, **Fedele, J.J.**, **Kleverlaan, K.** and **Pederson, K.H.** (2016) Morphodynamics of supercritical turbidity currents in the channel-lobe transition zone. *Adv. Nat. Technol. Hazards Res.*, 469–478. https://doi.org/10.1007/978-3-319-20979-1_47.

Prather, B.E., **Pirmez, C.**, **Sylvester, Z.** and **Prather, D.S.** (2012) Stratigraphic response to evolving geomorphology in a submarine apron perched on the upper Niger Delta slope. In: *Application of the Principles of Seismic Geomorphology to Continental-slope and Base-of-slope Systems: Case Studies From Seafloor and Near-seafloor Analogues* (Eds Prather, B.E., Deptuck, M.E., Mohrig, D., van Hoorn, B. and Wynn, R.B.), *SEPM (Society for Sedimentary Geology), Special Publication*, **99**, 145–161.

Prélat, A., **Hodgson, D.M.** and **Flint, S.S.** (2009) Evolution, architecture and hierarchy of distributary deep-water deposits: a high-resolution outcrop investigation from the Permian Karoo Basin, South Africa. *Sedimentology*, **56**, 2132–2154.

Recouvreur, A., **Fabregas, N.**, **Mulder, T.**, **Hanquiez, V.**, **Fauquembergue, K.**, **Tournadour, E.**, **Gillet, H.**, **Borgomano, J.**, **Poli, E.**, **Kucharske, J.** and **Wilk, S.** (2021) Geomorphology of a modern carbonate slope system and associated sedimentary processes: example of the giant great Abaco canyon, Bahamas. *Sedimentology*, **68**, 266–293.

van Rijn, L.C. (1993) *Principles of Sediment Transport in Rivers, Estuaries and Coastal Seas*. Aqua Publications, Amsterdam, 790 pp.

Robert McNeel & Associates (2010) *Rhinoceros 3D, V6.0*. Robert McNeel & Associates, Seattle, WA.

Rohais, S., **Bailleul, J.**, **Brocheray, S.**, **Schmitz, J.**, **Paron, P.**, **Kezirian, F.** and **Barrier, P.** (2021) Depositional model for turbidite lobes in complex slope settings along transform margins: the Motta san Giovanni formation (Miocene – Calabria, Italy). *Front. Earth Sci.*, **9**, 766946.

Saller, A., **Werner, K.**, **Sugiaman, F.**, **Cebastiant, A.**, **May, R.**, **Glenn, D.** and **Barker, C.** (2008) Characteristics of Pleistocene deep-water fan lobes and their application to an upper Miocene reservoir model, offshore East Kalimantan, Indonesia. *AAPG Bull.*, **92**, 919–949.

Schnyder, J.S.D., **Eberli, G.P.**, **Betzler, C.**, **Wunsch, M.**, **Lindhorst, S.**, **Schiebel, L.**, **Mulder, T.** and **Ducassou, E.** (2018) Morphometric analysis of plunge pools and sediment wave fields along western great Bahama Bank. *Mar. Geol.*, **397**, 15–28.

Shields, A. (1936) *Anwendung der Aehnlichkeitsmechanig und der Turbulenzforschung auf die Geschiebebewegung*. Mitteilungen der Preußischen Versuchsanstalt für Wasserbau und Schiffbau 26. Technische Hochschule Berlin, Berlin, 25 pp.

Soutter, E.L., **Kane, I.A.**, **Fuhrmann, A.**, **Cumberpatch, Z.A.** and **Huuse, M.** (2019) The stratigraphic evolution of onlap in siliciclastic deep-water systems: autogenic modulation of allogenic signals. *J. Sediment. Res.*, **89**, 890–917.

Soutter, E.L., **Bell, D.**, **Cumberpatch, Z.A.**, **Ferguson, R.A.**, **Spychala, Y.T.**, **Kane, I.A.** and **Eggenhuisen, J.T.** (2021) The influence of confining topography orientation on experimental turbidity currents and geological implications. *Front. Earth Sci.*, **8**, 1–25.

Spychala, Y.T., **Hodgson, D.M.**, **Flint, S.S.** and **Mountney, N.P.** (2015) Constraining the sedimentology and stratigraphy of submarine intraslope lobe deposits using exhumed examples from the Karoo Basin, South Africa. *Sediment. Geol.*, **322**, 67–81.

Spychala, Y.T., **Eggenhuisen, J.T.**, **Tilston, M.** and **Pohl, F.** (2020) The influence of basin setting and turbidity current properties on the dimensions of submarine lobe elements. *Sedimentology*, **67**, 3471–3491.

Stevenson, C.J., **Jackson, C.A.L.**, **Hodgson, D.M.**, **Hubbard, S.M.** and **Eggenhuisen, J.T.** (2015) Deep-water sediment bypass. *J. Sediment. Res.*, **85**, 1058–1081.

Stevenson, C.J., **Feldens, P.**, **Georgiopoulou, A.**, **Schönke, M.**, **Krastel, S.**, **Piper, D.J.W.**, **Lindhorst, K.** and **Mosher, D.** (2018) Reconstructing the sediment concentration of a giant submarine gravity flow. *Nat. Commun.*, **9**, 1–7.

Symons, W.O., **Summer, E.J.**, **Paull, C.K.**, **Cartigny, M.J.B.**, **Xu, J.P.**, **Maier, K.L.**, **Lorenson, T.D.** and **Talling, P.J.** (2017) A new model for turbidity current behavior based on intergration of flow monitoring and precision coring in a submarine canyon. *Geology*, **45**, 367–370.

Talling, P.J., **Baker, M.L.**, **Pope, E.L.**, **Ruffell, S.C.**, **Jacinto, R.S.**, **Heijnen, M.S.**, **Hage, S.**, **Simmons, S.M.**, **Hasenhündl, M.**, **Heerema, C.J.**, **McGhee, C.**, **Apprioual, R.**, **Ferrant, A.**, **Cartigny, M.J.B.**, **Parsons, D.R.**, **Clare, M.A.**, **Tshimanga, R.M.**, **Trigg, M.A.**, **Cula, C.A.**, **Faria, R.**, **Gaillot, A.**, **Bola, G.**, **Wallance, D.**, **Griffiths, A.**, **Nunny, R.**, **Urlaub, M.**, **Peirce, C.**, **Burnett, R.**, **Neasham, J.** and **Hilton, R.J.** (2022) Longest sediment flows yet measured show how major rivers connect efficiently to deep sea. *Nat. Commun.*, **13**, 4193.

Van der Merwe, W.C., **Hodgson, D.M.**, **Brunt, R.L.** and **Flint, S.S.** (2014) Depositional architecture of sand-attached and sand-detached channel-lobe transition zones on an exhumed stepped slope mapped over a 2500 km^2 area. *Geosphere*, **10**, 1076–1093.

Wynn, R.B., **Kenyon, N.H.**, **Masson, D.G.**, **Stow, D.A.V.** and **Weaver, P.P.E.** (2002) Characterization and recognition of deep-water channel-lobe transition zones. *AAPG Bull.*, **86**, 1441–1462.

Xu, J.P. (2010) Normalized velocity profiles of field-measured turbidity currents. *Geology*, **38**, 563–566.

Xu, J.P., **Noble, M.A.** and **Rosenfeld, L.K.** (2004) In-situ measurements of velocity structure within turbidity currents. *Geophys. Res. Lett.*, **31**, 1–4.

Xu, J.P., **Sequerios, O.E.** and **Noble, M.A.** (2014) Sediment concentrations, flow conditions, and downstream evolution of two turbidity currents, Monterey canyon, USA. *Deep Sea Res. I.*, **89**, 11–34.

Zhang, Y., **Liu, Z.**, **Zhao, Y.**, **Colin, C.**, **Zhang, X.**, **Wang, M.**, **Zhao, S.** and **Kneller, B.** (2018) Long-term in situ observations on typhoon-triggered turbidity currents in the deep sea. *Geology*, **46**, 675–678.

Manuscript received 28 March 2022; revision accepted 20 December 2022

Supporting Information

Additional information may be found in the online version of this article:

Appendix S1:

1 Notation and abbreviations

2 Grain-size data

3 UVP Parameters

4 Discharge data

5 Remaining concentration plots

6 Remaining densimetric Froude number plots

7 Remaining shear velocity plots

8 Remaining Rouse number plots

9 Remaining Potential and Kinetic energy plots

10 Channel deposit volume calculations

11 Remaining colour maps of basin deposits

12 Grain-size data